Surface & Coatings Technology 489 (2024) 131042

Contents lists available at ScienceDirect

Surface & Coatings Technology

journal homepage: www.elsevier.com/locate/surfcoat

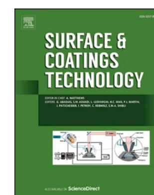

Full Length Article

# Porous-anodic-alumina-templated Ta-Nb-alloy/oxide coatings via the magnetron-sputtering/anodizing as novel 3D nanostructured electrodes for energy-storage applications

Alexander Mozalev [a,b,*], Maria Bendova [a,b], Francesc Gispert-Guirado [c], Eduard Llobet [d], Hiroki Habazaki [e]

[a] Department of Microelectronics, Faculty of Electrical Engineering and Communication, Brno University of Technology, Technicka 10, 616 00 Brno, Czech Republic
[b] CEITEC – Central European Institute of Technology, Brno University of Technology, Purkynova 123, 61200 Brno, Czech Republic
[c] SRCiT, University Rovira i Virgili, Av. Paisos Catalans 26, 43007 Tarragona, Catalonia, Spain
[d] MINOS, University Rovira i Virgili, Av. Paisos Catalans 26, 43007 Tarragona, Catalonia, Spain
[e] Graduate School of Chemical Sciences and Engineering, Hokkaido University, Sapporo, Hokkaido 060-8628, Japan

ARTICLE INFO

*Keywords:*
Porous anodic alumina
Tantalum-niobium alloy
Anodic oxide films
3D nanostructures
Electrolytic capacitor

ABSTRACT

The Ta-52 at.%Nb thin alloy films were magnetron sputter-deposited over a low-aspect-ratio nanoporous anodic-alumina template formed in 0.05 M tartaric acid solution at 250 V and modified by the pore-widening technique to enlarge the pores up to ~500 nm. The alloy coated the pores evenly, thus forming a 3D continuous conducting nanofilm on the template. Partially anodizing the templated alloy in a borate buffer solution of pH 7.5 generated a compact amorphous mixed-oxide anodic film thickening proportionally to the applied voltage. It was revealed that the oxide on the Ta-52 at.%Nb alloy grows with a slower migration of $Ta^{5+}$ ions relative to $Nb^{5+}$ ions, resulting in mixing $Ta_2O_5$ and $Nb_2O_5$ in the film depth and forming a few-nm-thick $Nb_2O_5$ outmost layer. The unique migration of $Ta^{4+}$, $Ta^{3+}$, $Nb^{4+}$, and $Nb^{3+}$ ions is assumed accountable for forming corresponding sub-oxides in the 3D anodic film in contrast to a flat Ta-52 at.%Nb alloy film used as a reference. The 3D anodic films behave as an *n*-type semiconductor with a low donor density $N_d = \sim 2 \times 10^{18}$ $cm^{-3}$, appropriate for dielectric applications. An unusual two-layered structure with a sharp electrical interface revealed in the 3D oxide films anodized to 30–130 V, comprising a low-resistivity layer superimposed on the high-resistivity layer, is explained by an immobile negative space charge in the outer film part. The air-annealing at moderate temperatures releases the space charge and transforms the two layers into a high-resistivity single layer having substantially improved dielectric properties and thermostable (up to 250 °C) capacitance of 1.2 μF $cm^{-2}$ achieved for the film anodized to practical 50 V. The 3D films having up to 4.5 times enlarged effective surface area can be utilized as novel metal/oxide nanostructured electrodes for electrolytic microcapacitors suitable for classical electronic circuits and energy-storage applications.

## 1. Introduction

Among the various engineered nanostructured materials, 3D nanostructures have become most appropriate for constructing high-performance nano- and microdevices [1]. They seem indispensable for designing electrodes for electrochemical energy conversion and storage devices, including various types of capacitors, which ideally should combine high energy storage and power density. An effective strategy to improve the energy storage density of supercapacitors, electrostatic capacitors, and electrolytic capacitors is enlarging the surface area of active materials in contact with electrolyte or solid conducting electrodes by engineering the materials as 3D nanostructures. These are commonly understood as assemblies of 1D nanomaterials (nanowires, nanotubes, or nanorods), combinations of 2D nanomaterials (nanosheets or nanoflakes), nanotubular structures, and hierarchically constructed nanomaterials [1]. However, arrays of high-aspect-ratio 1D

* Corresponding author at: Department of Microelectronics, Faculty of Electrical Engineering and Communication, Brno University of Technology, Technicka 10, 616 00 Brno, Czech Republic.

*E-mail addresses:* mozalev@vutbr.cz (A. Mozalev), bendova@vutbr.cz (M. Bendova), francesc.gispert@urv.cat (F. Gispert-Guirado), eduard.llobet@urv.cat (E. Llobet), habazaki@eng.hokudai.ac.jp (H. Habazaki).

https://doi.org/10.1016/j.surfcoat.2024.131042
Received 13 April 2024; Received in revised form 6 June 2024; Accepted 20 June 2024
Available online 26 June 2024
0257-8972/© 2024 The Authors. Published by Elsevier B.V. This is an open access article under the CC BY license (http://creativecommons.org/licenses/by/4.0/).

nanostructures tend to agglomerate or cluster because of mechanical weakness and surface interaction forces. The agglomeration lowers the effective specific surface area and increases the ionic transport resistance of the electrode, which worsens the performance of supercapacitors. 3D nanoporous or nanotubular materials [1] have proved to be the solution after their appropriate functionalization, such as anodically formed nanotubular $TiO_2$ [2]. Since first reports dated back to the 1990s [3], nanoporous membranes or films made of chemically inert, physically stable, and electrically non-conductive (dielectric) materials, such as porous anodic alumina (PAA), have emerged as nanostructured templates for hosting and shaping various functional materials [4]. Since early work by Moskovits et al. [5], PAA membranes, sheets, or layers on substrates have been synthesized and tested as self-organized nanoporous matrixes for accommodating multilayered deposits as elements of 3D electrostatic (non-polarized) capacitors first made by chemical vapor deposition (CVD) [5], which was later replaced by more capable atomic layer deposition (ALD) [6–8].

Such a 3D electrostatic capacitor combining a PAA template with the ALD-made ultrathin multilayers inside the pores typically comprised a top conductor electrode, a dielectric layer, and a bottom conductor electrode [5]. In one of the later designs, a thin layer of aluminum-doped zinc oxide (AZO), 3 nm thick, was utilized as both the top and bottom electrodes, while a $SiO_2/TiO_2/SiO_2$ trilayer, 9 nm thick, was the capacitor dielectric [9]. In several other works, AZO/$Al_2O_3$/AZO [10,11], TiN/$Al_2O_3$/TiN [12], or TiN/$HfO_2$/TiN [13] nanolaminates made by ALD inside the PAA nanopores complemented the variety of 3D capacitor designs. Although some of such capacitors have reportedly achieved equivalent planar capacitance of up to ~100 μF $cm^{-2}$ with a 10-micron thick template and significantly enlarged energy storage density [12], their consideration for practical applications has been limited to energy-storage electrostatic capacitors because of the low operational and breakdown voltage, high leakage currents, and very low working frequencies (tens of Hertz). Moreover, the AZO layer did not serve well as the conducting electrode because of the abstracted electron transfer between the AZO and the contact pads, its semiconducting nature, and few-nanometer limited thickness resulting in insufficient, dispersed, and temperature-dependent conductivity along the pore length and across the PAA surface [9]. Whatever the capacitor design was, the frequent shorting of the electrodes and poor manufacturing yield further limited the application potential of the PAA-ALD technology for electrostatic capacitors.

What has remained beyond the capability of the PAA-ALD technology is an electrolytic (polarized) capacitor, whose anode is made of a metal that can be anodized to form an insulating oxide layer that acts as the capacitor dielectric. A solid, liquid, or gel electrolyte covers the surface of this oxide layer and serves as the capacitor cathode. Electrolytic capacitors are particularly suitable in electronic circuits for passing or bypassing signals, noise filtering, or decoupling. Besides, because of their potential for a large specific volumetric capacitance, electrolytic capacitors can store large amounts of energy, substantially overperforming electrostatic capacitors in energy-storage applications and supercapacitors in dealing with current fluctuations.

In pursuit of energy storage devices and systems smaller and lighter, the development of 3D nanostructured electrolytic capacitors may contribute substantially to the future high-yield production of large-value electrolytic microcapacitors suitable for on-chip integration [14]. It should be noted that the challenge cannot be met with the ALD approach because it is not appropriate for depositing metal layers and any layers thicker than a few nanometers.

In the present work, we have developed an alternative, ALD-unemploying, facile, and highly reproducible technology for 3D nanostructured electrodes for electrolytic microcapacitors that combines the formation of relatively large-nanopore PAA templates with the DC magnetron sputter-deposition of metal or metal-alloy layers and subsequent partial anodizing of the deposit for forming continuous anodic-oxide layers of various thicknesses to serve as the capacitor dielectric. To this end, we adopted a set of technological, electrical, and electrolytic conditions for forming a low-aspect-ratio PAA template in which the pore population density, pore size, and pore depth were balanced to achieve a substantial rise in the open film surface. Recently, niobium capacitors were developed and became an alternative and competing technology for tantalum electrolytic capacitors [15]. In the present work, we mixed tantalum with niobium to create a solid solution with approximately equal concentrations of the components, striving to improve the properties of individual metal oxides toward better-quality dielectrics based on previous reports justifying the advantages of such mixing [16–19]. For the first time, the Ta-Nb alloy was magnetron-sputter deposited over the PAA template in such a way that it conformally coated the pores, leaving the pore necks unblocked by the deposit and allowing anodizing voltages up to 130 V. The PAA-templated, anodized, and annealed alloy layers were examined by scanning electron microscopy (SEM), X-ray photoelectron spectroscopy (XPS), X-ray diffraction (XRD), electrochemical impedance spectroscopy (EIS), and Mott-Schottky analysis to gain an insight into the formation-structure-property relationship of these unique 3D nanostructures and assess their applicability as the electrodes for electrolytic microcapacitors.

## 2. Experimental part

### 2.1. PAA fabrication

Specimens of aluminum foil (99.99 %, as rolled, Goodfellow), 200 μm thick, cut to 20 mm × 30 mm, were employed as the starting material. To remove surface defects and the traces of the rolling mill and to have a reproducible starting surface, the specimens were degreased in acetone and electropolished individually at 200 mA $cm^{-2}$ in a mixture of perchloric and acetic acids, rinsed in running distilled water, and dried in a warm air stream. The specimens were anodized in 0.05 M tartaric acid electrolyte at 23 °C. This electrolyte was selected due to the high anodizing voltages that can be attained at the steady-state stage of PAA growth (~250 V) associated with a sizeable interpore distance (>600 nm) and wide pore diameters (~60 nm), which may be further expanded by post-anodizing chemical etching [20,21]. In the course of this study, citric-acid solutions of various concentrations, enabling the anodizing voltages as high as 350–420 V [22–24], were also tried for PAA fabrication directly on an Al foil and on an Al thin film magnetron-sputtered on a Si wafer. The comparative results and discussion justifying the choice of specific anodizing conditions for generating the PAA layers with the most appropriate geometry are available in the ESI file (Figs. S3–S6 and relevant text). Anodizing the electropolished Al foil was carried out in two consequential steps to grow a small-aspect-ratio (~1.5) PAA layer with improved pore regularity, enlarged pore outlets, and increased effective surface area at the electrolyte/film interface. In the first step, outlined in Fig. 1a, the specimen was polarized in 0.05 M tartaric acid solution at a constant current density of 6 mA $cm^{-2}$ for 20 min, during which the voltage attained a steady-state value of 250 V. Then, the PAA layer was selectively dissolved away (Fig. 1b) [25], and the specimen was anodized again in the same electrolyte (Fig. 1c) by sweeping the voltage at a rate of 2 V $s^{-1}$ to 250 V, then holding the voltage for 5 min. The pores in the as-anodized PAA template were expanded by chemical etching in a stirred aqueous solution of 0.6 M $H_3PO_4$ and 0.15 M $CrO_3$ [26] kept at 65 °C for 20 min to achieve the mean pore diameter of about 500 nm, as sketched in Fig. 1d.

### 2.2. Ta-Nb alloy coating

The Ta-Nb alloy coatings on the PAA template and thermally oxidized Si wafers were prepared by DC magnetron sputtering in a Vacuum Products SP-2C system. For forming a Ta-Nb alloy layer containing approximately 50 at.% niobium, a disk of 99.9 % pure niobium of 100 mm in diameter was used as the target, on which four disks of

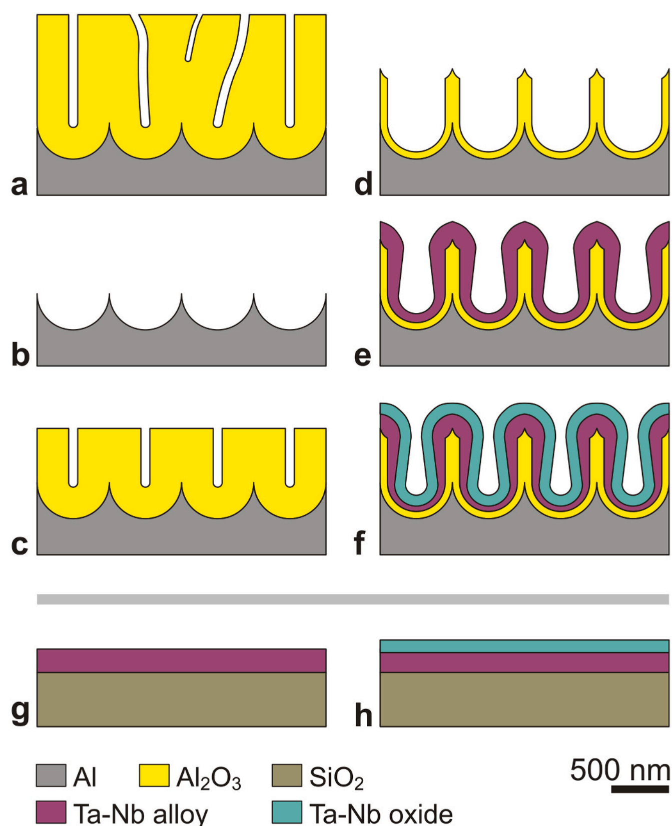


**Fig. 1.** Schematics of the main steps for forming 3D and flat Ta-Nb mixed anodic oxides on a PAA template and a $SiO_2$/Si wafer, respectively: (a) the formation of porous anodic alumina (PAA) layer on a polished Al foil, (b) the selective dissolution of the PAA layer to pattern the foil surface, (c) the second anodizing of the patterned Al foil, (d) the pore widening, (e) the magnetron sputter-deposition of a Ta-Nb alloy on the PAA template, (f) the anodizing of the templated Ta-Nb alloy to 50 V (as an example). Panels (g) and (h) depict the sputter-deposition and anodizing to 50 V of a flat layer of Ta-Nb alloy.

pure 99.9 % tantalum of 20 mm in diameter were placed symmetrically to cover about 50 % of the erosion region. All alloy films were deposited at the same time. The sputtering chamber was evacuated to ~5 × $10^{-5}$ Pa, and then sputtering was conducted in 99.999 % argon (~0.3 Pa) at 0.5 A for 600 s to obtain an alloy film of 200 nm thickness when measured on a flat substrate. During the deposition, the specimen holders were rotated around a central axis of the chamber and their axis to generate alloy films of uniform thickness and composition. The deposition angle for the PAA template and Si wafers was 0° relative to the substrate normal. Fig. 1e, g depicts what was expected to result from the efforts.

### 2.3. Ta-Nb alloy anodizing

The Ta-Nb alloy coating on the PAA substrate (hereafter the '3D' film) and the Ta-Nb alloy coating on an oxidized Si wafer (hereafter the 'flat' film) were further anodized to various voltages, $U_a$, from 5 up to 180 V, to grow nanostructured 3D and thin-film flat anodic oxides of increasing thicknesses (Fig. 1f, h). First, the specimen surface was patterned with PMMA to leave openings of 10 mm × 6 mm to be soaked with the anodizing solution. A droplet of the electrolyte was put in a selected opening using a pipet, and a spade-like Au counter electrode contacted the droplet top. The droplet was held between the anode (the specimen) and the counter electrode by surface tension. A schematic view and digital photos of the anodizing setup are shown in ESI, Fig. S1. Compact anodizing of the alloy was carried out in borate buffer solution (0.5 M $H_3BO_3$ and 0.05 M $Na_7B_4O_7$, pH 7.5) at 22 °C at a constant current density of 1 mA $cm^{-2}$ until the voltage attained a set value, followed by holding the voltage for 10 min until the current decayed to its leakage value. The conditions for alloy anodizing were selected based on previous experience with growing dielectric anodic films on valve metals [27,28]. Thermal treatment of selected specimens was performed in an ambient atmosphere at temperatures ranging from 100 to 300 °C for 60 min.

### 2.4. Chemical and structural analyses

**SEM**. The surfaces and cross sections of the 3D and flat alloys and corresponding anodic films were examined in a MIRA II (TESCAN) scanning electron microscope operated at 30 kV. The microscope had an InBeam detector for secondary electrons; therefore, no charge-reducing conducting layers were deposited before the observation. **XPS**. The chemical composition of the 3D and flat alloys and anodic films was analyzed by XPS in a Kratos Axis Ultra DLD and Kratos Axis Supra spectrometers employing a monochromatic Al Kα source. Typical operating pressures were $<1.3 \times 10^{-9}$ mbar. The emitted electrons were detected by a hemispherical analyzer at fixed pass energies of 160 and 20 eV for the survey and high-resolution spectra, respectively. The Kratos charge neutralizer system was used for all specimens. Sputter-cleaning was performed using an argon-ion beam of 3 kV provided by a standard ion gun with a filament emission current of 2.5 μA scanned over a surface window of 2 mm × 2 mm for 230 s, resulting in slight surface etching. The sputtering-beam incidence angle was 45° relative to the substrate. CasaXPS software version 2.3.24PR1.0 was used for spectra analysis. GL (30) profiles, defined in CasaXPS, were used for all components besides the metallic core lines of Nb 3d and Ta 4f, for which asymmetric profiles in the form of LA (1.2, 3.3, 12) and LA (1.1, 4, 25) were used, respectively. A standard Shirley background was used in all fitted spectra. Spectra from all samples were charge corrected to give the adventitious C 1s spectral component (C–C, C–H) binding energy of 284.8 eV. The deconvolution of C 1s spectra was performed as described in previous works [29–32] and is shown in ESI. The quantitative analysis was performed for the narrow spectra using the relative sensitivity factors from CasaXPS (referenced to F 1s) suitable for Kratos Axis Ultra. **XRD**. Diffraction patterns of the 3D and flat alloys and anodic films were taken from a Bruker-AXS D8-Discover diffractometer operated at 40 kV and 40 mA to generate CuKα radiation. An X-ray collimator of a 500 μm system allowed the analysis of a mean area represented by an ellipsoid with a constant short axis of 500 μm and a variable long axis of 600–1500 μm. The VÅNTEC-500 detector (silicon strip technology, active area of 30 cm × 30 cm, frame size of 2048 pixels × 2048 pixels) was placed at a 15-cm distance from the sample. Sixteen frames were collected in reflection mode covering 20–90° $2\theta$ with a step size of 0.8° to obtain a conventional 2D diffractogram suitable for Rietveld analysis [33]. The exposure time was 300 s per frame, and it was $\gamma$-integrated to generate the $2\theta$ vs. intensity diffractogram. The experimental diffractograms were fitted with the crystal structure [34] for the phases identified using TOPAS 6.0 software (Bruker AXS GmbH, 2017) [35].

### 2.5. Electrochemical analysis

All EIS measurements were carried out using an Autolab PGSTAT204 Potentiostat/Galvanostat with a FRA32M module (Metrohm) in the borate buffer at 22 °C with the same two-electrode setup utilized for the anodizing (Fig. S1). The working electrode was the remaining (non-anodized) alloy layer beneath the anodic films. The EIS characterization of the 3D and flat anodic films was performed by applying a sinusoidal perturbation of 100 mV in a frequency range of 1.0 MHz to 0.01 Hz. All EIS measurements were conducted at 0.0 V except those performed under various bias potentials, $U_b$. Mott-Schottky experiments were performed for selected anodic films by measuring EIS in a narrower frequency range (1.0 MHz–0.1 Hz) at potentials from +5.0 to −1.0 or −3.0 V in 1.0-V steps. The experimental EIS data were analyzed using

computer simulation and fitting software Autolab NOVA and Gamry Echem Analyst. The entire frequency range was used for fitting with an equivalent electrical circuit(s) containing a constant phase element (CPE) in parallel with a resistor, from which the capacitances were extracted $C = Y_0^{1/n} \cdot R_p^{(1-n)/n}$ [36]. Unless stated otherwise, all area-related physical quantities will be related to the apparent surface area exposed to anodizing or EIS measurements [37].

## 3. Results

### 3.1. Anodizing behavior of the Ta-Nb coatings

As a practical example, the comparative current-time and voltage-time behaviors for anodizing the 3D and flat alloy films up to $U_a$ = 50 V (hereafter, the '50-V anodic films') are shown in Fig. 2. The voltage transients at the commencement of anodizing (up to 12 V) are shown in Fig. S2. It should be noted that the two samples had the same (patterned with PMMA) apparent surface area (0.6 $cm^2$), as described in Section 2.3, and the same current (0.6 mA) was applied for the galvanostatic polarization of each sample, which enables direct comparative analysis of the voltage transients during the constant-current anodizing. The systematic voltage rise under the constant-current polarization from 3 to 50 V is characteristic of anodic films thickening proportionally to the applied voltage with a nearly 100 % current efficiency under the high field. The initial voltage surge, more pronounced for the 3D alloy, arises from an air-formed film on top of the alloys. Apparently, such a layer is relatively thicker in the 3D alloy, manifested by a voltage jump up to 3 V, before the steady growth begins, though at a substantially reduced rate compared with the flat alloy anodizing. Assuming comparable formation efficiencies for the two films, the difference in the slopes of the curves after the initial voltage surges can be explained by dissimilar surface areas in contact with the electrolyte (hereafter, the 'effective' area) [38]. Moreover, the voltage rises substantially slower and at a progressively increasing rate in the range of 3 to 5 V during the anodizing of the 3D alloy (Fig. S2). The voltage rate becomes relatively stable only beyond ~10 V and barely changes up to the set limit. The features related to the enlarged effective surface area in the 3D alloy will be thoroughly considered later in the text.

### 3.2. Ta-Nb alloy/oxide film morphology

SEM images in Fig. 3 show the surfaces and corresponding cross sections of the PAA-templated Ta-Nb alloy as-deposited and partially anodized, pointing out the main steps of the fabrication process (outlined in Fig. 1) such as the preparation of PAA substrate with widened pores followed by the sputter-deposition of Ta-Nb alloy and its anodizing to a practical voltage of 50 V. Table 1 reviews the major geometrical parameters of the PAA template before and after the pore-widening procedure and following the deposition of the Ta-Nb alloy and its anodizing to 50 V. The whole collection of images recorded after each formation step outlined in Fig. 1 is available in the ESI file (Fig. S3).

The PAA cell walls that remain after the pore widening (Fig. 3, left column) seem to be the thinnest to expect mechanical stability of the template. The pore outlets are nearly round, while the PAA cell walls protrude outward, especially at the triple interconnection points at the cell boundaries. The widened pores have an aspect ratio (depth-to-diameter ratio) of ~1.5. The pore walls and bottoms are smooth and featureless at the SEM resolution. The pores, cell walls, surface concaves, funnel-like pore outlets, and the multi-concaved morphology of the film top all together increase the outer film surface. Based on the SEM observation, the template's effective surface is about 4 times the apparent specimen surface.

One may see that the deposit inside the pores (Fig. 3, middle column) has a nanosized grain structure, which expands toward the pore outlets. The thickness of the thinnest parts of the deposit inside the pores measures ~60 nm. The areas of the deposit covering the pillar-like surface of the PAA substrate have a significantly more pronounced grain structure, transforming into stacks of rectangle nanosheets measuring between ~50 and ~20 nm. The overall thickness of the alloy beyond the pores reaches ~200 nm in its thickest parts. The thickness of the 50-V anodic oxide measures ~100 nm, while the remaining (non-anodized) alloy layer measures ~15 nm in its thinnest parts (the pore walls and bottoms, Fig. 3, right column). Therefore, the remaining alloy layer covers the entire template interior and should perform as a fully functional conducting bottom electrode. The 50-V formed anodic oxide has an entirely smooth surface and uniform thickness across the template, swelling due to the oxide volume growth, losing the initial roughness of the deposited alloy, and not revealing any 'visible' compositional gradient across the film section.

### 3.3. Chemical composition of Ta-Nb alloy/oxide films

The specimens analyzed were the (1) flat as-deposited Ta-Nb alloy, (2) flat Ta-Nb alloy anodized to 50 V, and (3) 3D Ta-Nb alloy anodized to 50 V (Fig. 4). Mostly, XP spectra were recorded on the as-prepared surfaces. The as-deposited alloy was also examined after a short sputter-cleaning cycle to remove carbon contamination and air-formed oxides. C, O, Nb, Ta, and Si were identified in the survey spectra of all samples (Si was not present after the sputter-cleaning cycle). Narrow-scan C 1s, O 1s, Nb 3d, and Ta 4f spectra were collected to analyze their core levels and bonding states. The experimental and fitted Nb 3d and Ta 4f spectra for the as-prepared surfaces are shown in Fig. 4. The C 1s, O 1s, and extended-range Ta 4f (15–40 eV) spectra are shown in Fig. S8. The spectra of the Ar-ion-sputtered initial alloy layer are presented in Fig. S7. A detailed description of spectra deconvolution is available in the ESI (including considerations of O 2s contributions in the Ta 4f spectra, Ta 4f loss peaks and Nb 4p transitions in the extended-range Ta 4f spectra, and deconvolution of O 1s spectra considering the adventitious carbon contribution, to obtain more precise O:(Ta + Nb) ratios).

The deconvolution of the Nb 3d and Ta 4f spectra of the flat alloy film (Fig. 4a, b) reveals the presence of a thin native oxide layer ($Nb^{5+}$, $Nb^{4+}$, $Ta^{5+}$, and $Ta^{4+}$ species) covering the metallic alloy ($Nb^0$ and $Ta^0$ species). The areas in the Nb 3d and Ta 4f regions (after subtracting the O 2s peak) were used to calculate the amount of Nb in the alloy, resulting in 52 at.% Nb (provided that at.%(Ta + Nb) = 100 %) for the as-received alloy surface.

The surface layer of the flat anodic film (Fig. 4c, d) is composed of a stoichiometric $Nb_2O_5$ (only $Nb^{5+}$ species are found in the Nb 3d spectrum) and a critically low amount of $Ta_2O_5$ (~0.3 at.% Ta, provided that at.%(Ta + Nb) = 100 %), whereas the possible presence of lower-

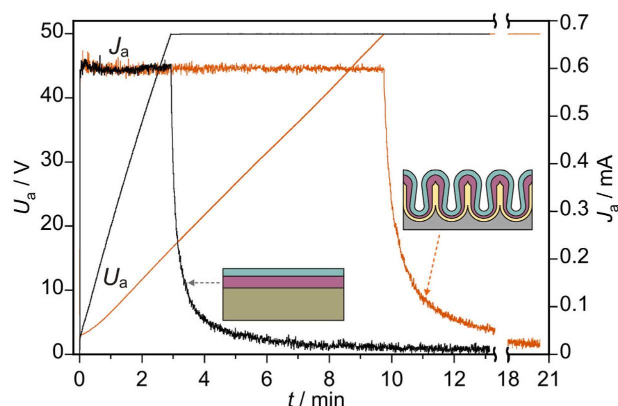


**Fig. 2.** The current density, $J_a$, and voltage, $U_a$, transients during anodizing the Ta-Nb alloy layers magnetron sputter-deposited over the PAA template formed at 250 V and $SiO_2$/Si wafer (as depicted in Fig. 1e, g). Anodizing was carried out in a combined mode, beginning with a constant-current polarization and continuing with a constant-voltage polarization after the voltage attained 50 V.

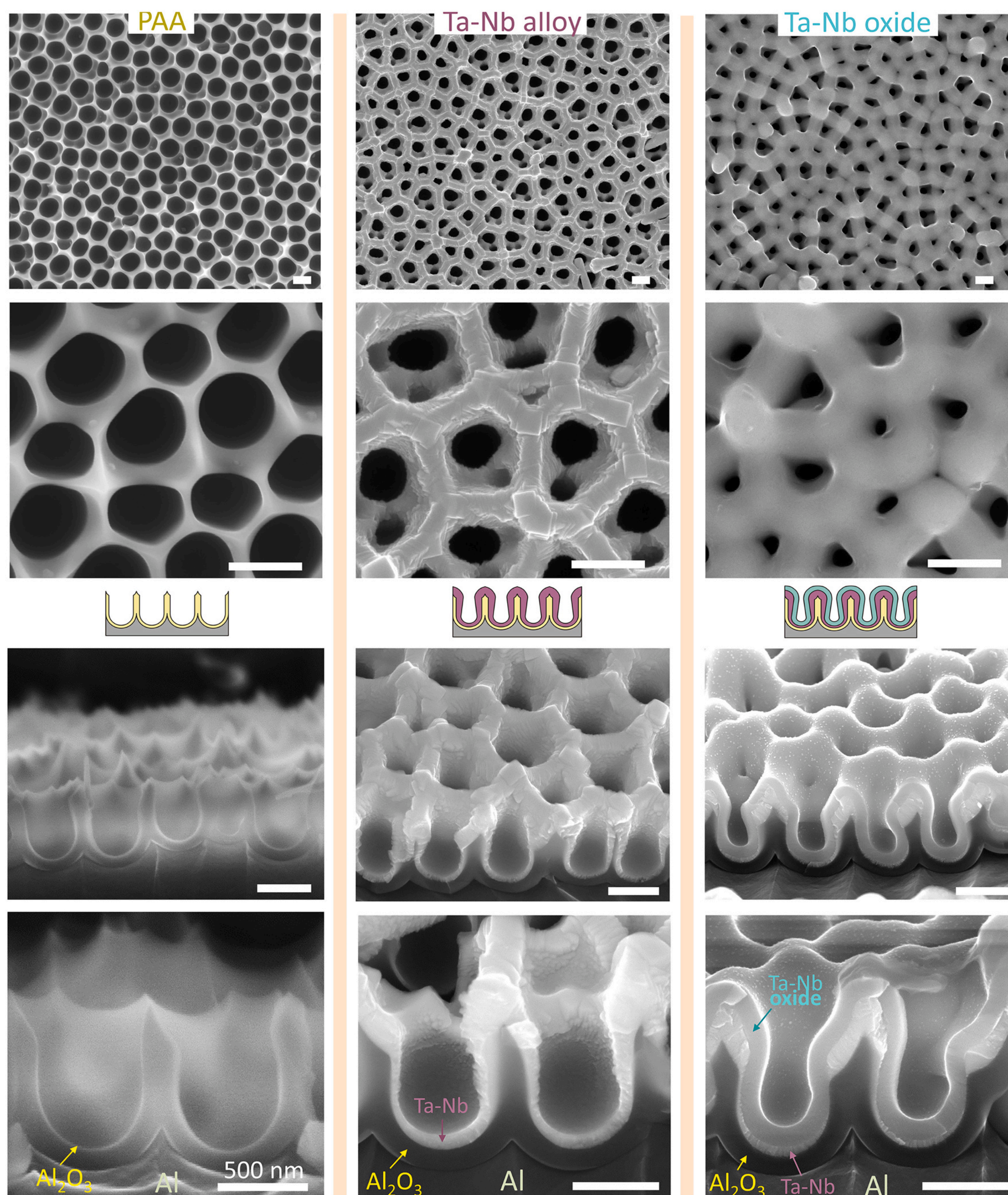


**Fig. 3.** SEM surface and cross-sectional views of (left column) the PAA template after the pore widening, (central column) the Ta-Nb alloy sputter-deposited over the pore-widened PAA template, and (right column) the PAA-templated Ta-Nb alloy anodized to 50 V (as depicted in Fig. 1).

**Table 1**
Mean geometrical parameters of the PAA template before and after the pore widening and Ta-Nb alloy deposition (measured in SEM images).

| PAA template as-anodized | | | PAA template after pore widening | | | Ta-Nb alloy coating | | Ta-Nb oxide (anodized to 50 V) | |
|---|---|---|---|---|---|---|---|---|---|
| Formation voltage, V | Pore diameter, nm | Pore density, $cm^{-2}$ | Pore diameter, nm | Pore depth, nm | Pore separation, nm | Thickness in pores, nm | Pore diameter, nm | Film thickness, nm | Pore diameter, nm |
| 250 | 80 ± 10 | $2.5 \times 10^8$ | 500 ± 15 | 750 ± 35 | 100 ± 15 | 60 ± 5 | 380 ± 40 | 100 ± 9.5 | 180 ± 30 |

valency Ta cations cannot be estimated from the Ta 4f spectrum. This indicates that the surface layer of the flat anodic film is composed of a pure stoichiometric $Nb_2O_5$ formed above a mixed Ta-Nb anodic-oxide layer. This finding agrees with the literature [39] describing the formation of a thin pure $Nb_2O_5$ outer layer on a thick anodic layer of mixed composition, grown on Ta-Nb alloys, originating from the faster outward migration of $Nb^{5+}$ ions relative to $Ta^{5+}$ ions [39]. For the Ta-52 at.%Nb alloy prepared in our study, the thickness of the pure $Nb_2O_5$ outer layer should take ~3 % of the total film thickness [39], which is ~3 nm for a 100 nm thick 50-V anodic film. This value is close to the depth

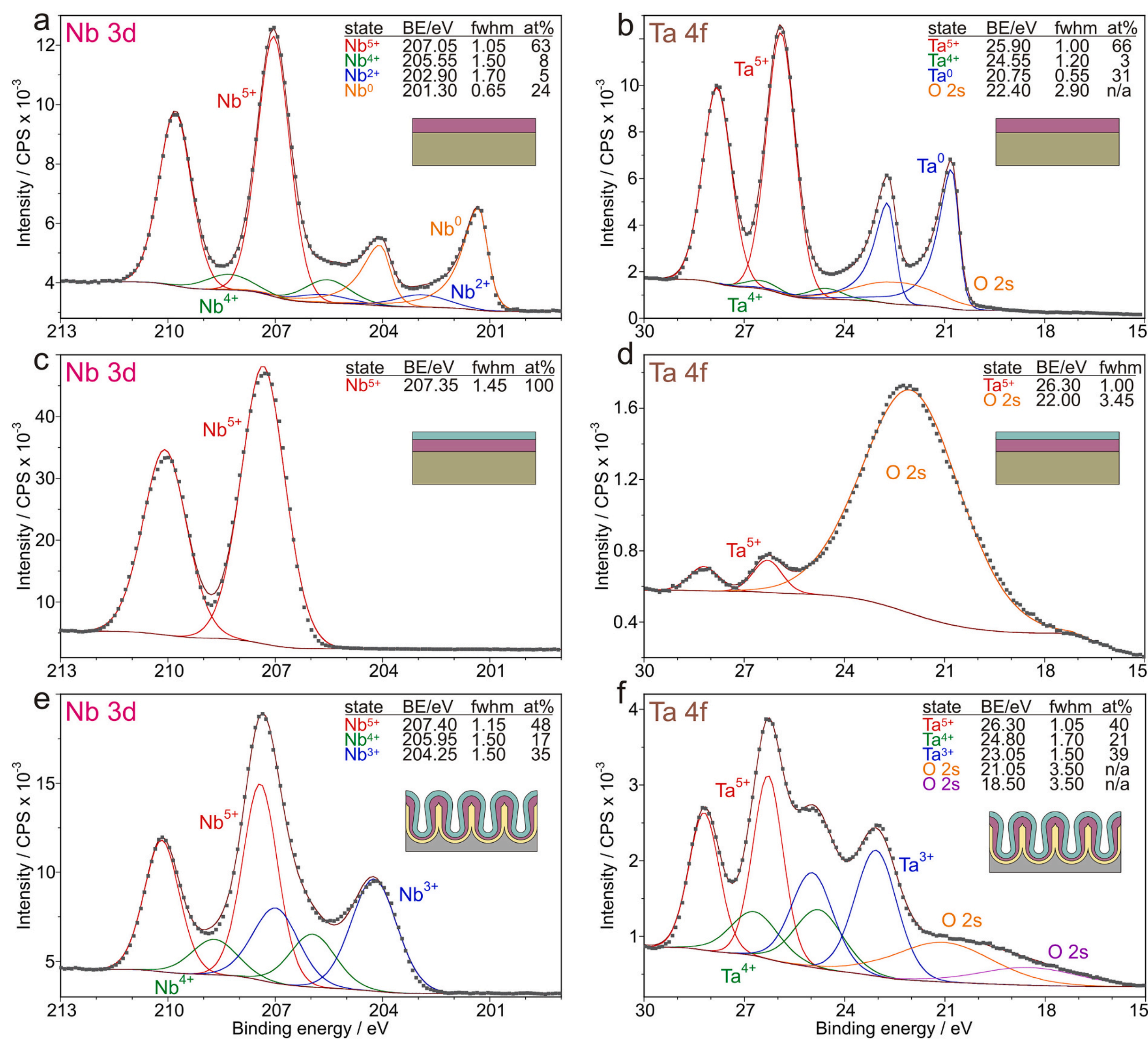


**Fig. 4.** Experimental and curve-fitted narrow-scan (left column) Nb 3d and (right column) Ta 4f XP spectra of the (a, b) flat Ta-Nb alloy film, (c, d) flat Ta-Nb alloy film anodized to 50 V, and (e, f) 3D alloy film anodized to 50 V.

sensitivity of XPS [40]; therefore, most of the photoelectrons are emitted from the thin pure $Nb_2O_5$ outer layer, while a few of them from the underlying mixed $Nb_2O_5$–$Ta_2O_5$ oxide, resulting in the small tantalum content observed at the film surface.

The 3D anodic film reveals more complex Nb 3d and Ta 4f spectra (Fig. 4e, f), which are deconvoluted with three relatively intense doublets, attributed to $Nb^{n+}$ and $Ta^{n+}$ cations with $n = 5$, 4, and 3. The Ta 4f spectrum also contains two smaller and broad O 2s peaks, whereas the low-BE O 2s peak may correlate with the unusually low-BE O 1s peaks in the corresponding O 1s spectrum (see ESI). The amount of the lower-valency cations is ~50–60 % from each element, underlying the high involvement of Nb and Ta suboxides in the surface layer of the 3D anodic film. The calculated amount of Ta is 21 at.% (provided that at.%(Ta + Nb) = 100 % after subtracting the O 2s components), which is higher than for the flat anodic film (0.3 at.% Ta) but still smaller than in the alloy (48 at.% Ta). It may be that cation migration in the anodic film on the PAA-supported Ta-Nb alloy differs from that in the flat anodic film, resulting in an intermediate Ta content. The average surface composition of the 3D anodic film is thus a highly substoichiometric niobium oxide (79 at.%) mixed with a highly substoichiometric tantalum oxide (21 at.%).

In summary, the XPS-determined Ta content in the anodic films is substantially lower than in the alloy (48 at.%), which is explained by a faster migration rate of $Nb^{5+}$ cations relative to $Ta^{5+}$ cations, resulting in the formation of a few-nm-thick relatively pure niobium-oxide outermost layer. Such a layer is thinner in the 3D anodic film since the Ta concentration at its surface (21 at.%) substantially exceeds that at the flat-film surface (0.3 at.%). Further, the 3D film substantially comprises tantalum and niobium suboxides (~50 % of all cations), whereas its flat counterpart contains only fully stoichiometric pentoxides. The unusually low-BE O 1s and O 2s peaks in the spectra of the 3D anodic film imply the presence of compositional extra features (assumingly extended amounts of electrolyte-derived anions), which may impact the films' electrical properties described in Section 3.5.

### 3.4. *Crystal structure of Ta-Nb alloy/oxide*

As a practical example, Fig. 5a, b shows the 2D and conventional diffractograms in the 20–90° 2$\theta$ angle range for the 3D Ta-52 at.%Nb alloy film before and after anodizing to 50 V. The crystal structures for all phases were identified using the ICSD database (FIZ, 2015); the main refined parameters and fitted X-ray diffractograms are available in the ESI.

The diffractograms in Fig. 5a and b are best interpreted with the

 

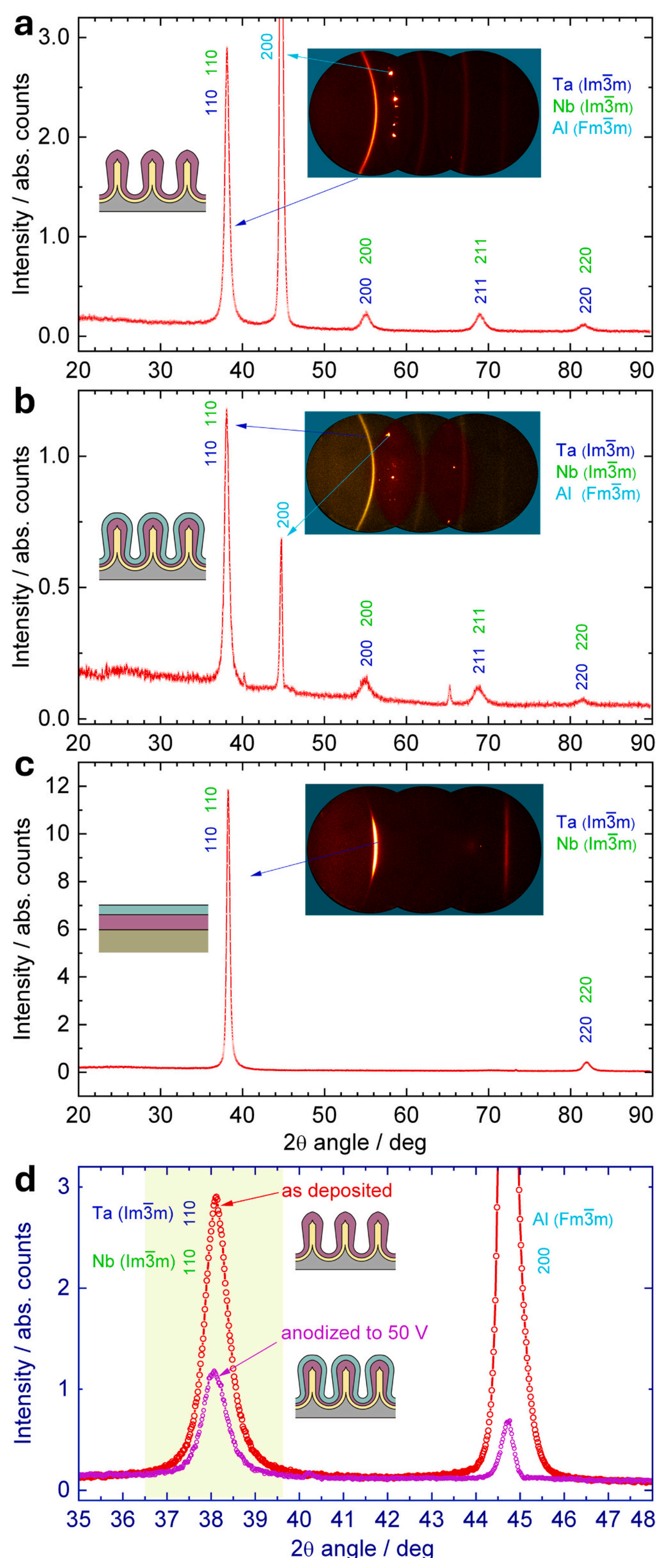


**Fig. 5.** 2D and conventional XRD diffractograms of the (a) as-deposited 3D Ta-52 at.%Nb alloy, (b) 3D Ta-52 at.%Nb alloy anodized to 50 V, (c) flat Ta-52 at.%Nb alloy anodized to 50 V. Panel (d) compares the intensities of (110) peaks in the as-deposited and 50-V anodized 3D Ta-52 at.%Nb alloy specimens as depicted in the sketches.

presence of metallic Ta (Nb) phase (Im$\overline{3}$m space group) and Al (Fm$\overline{3}$m) phase. The Al peak is obviously due to the aluminum foil used as the substrate. The foil has large, over 100 μm, monocrystalline grains, which diffract as spots instead of rings. As the diffractometer setup allows analyzing a small area, ~500 μm in diameter, a few Al crystallites diffract in contrast with a large number of the significantly smaller in size metallic Ta (Nb) nanocrystallites. Consequently, the intensities of Al peaks are not reproducible across the sample surface and vary widely depending on what grains interact with the microfocused X-ray beam. This consideration makes it impossible to estimate the wt% of the phases present using the Rietveld method. The presence of Ta (Nb) deduced from several peaks produced by the pointed-out reflections is due to the tantalum-niobium alloy layer deposited on the PAA template and partially remaining after the 50-V anodizing, as shown in SEM images of Fig. 3. Since the two components in the alloy are present in comparable concentrations and make a solid solution, it is impossible to differentiate between the Ta and Nb reflections because the two metals have the same crystal structure and nearly equal cell parameters ($a_{Nb}$: 3.3066 Å, $a_{Ta}$: 3.3058 Å, from ICDD cards 35–789 and 4–788). The mean size of the Ta-Nb crystallites before and after the anodizing is identical, 13.0 nm, calculated from (110) integral breadth. This consideration implies that the crystallinity of the remaining alloy layer is not affected by anodizing.

The 3D alloy reveals no long-range orientational order at the XRD resolution used. Fig. 5d compares the intensities of the (110) peaks for the as-deposited and 50-V anodized 3D alloy films. By calculating and comparing the refined scale factor (Rietveld parameter related to the diffracting mass) based on the (110) peaks for the two samples, it is estimated that 65 % of the initial alloy mass remains unoxidized after the 50-V anodizing. Considering the thickness of the sputter-deposited alloy layer, it is assessed that the 50-V anodizing does not entirely consume the alloy even in its thinnest parts on the pore walls and pore bottoms, as seen in the fragments of the cross-sectional SEM views in Fig. 3. Another important revelation from the XRD analysis is that both the 3D and flat anodic films (Fig. 5b, c) grow entirely amorphously since no crystalline peaks are detected. The field crystallization of anodic oxides is detrimental to capacitor applications due to the degradation of the electric properties associated with increasing leakage current and worsening dissipation factor [16,19]. As revealed in the previous work [19], the susceptibility of the Ta-Nb alloy to field crystallization increases with increasing niobium content in the alloy, being also affected by the initial film morphology, applied voltage, anodizing regime, formation electrolyte, temperature, and other factors. Our results show that the anodizing to 50–130 V of the PAA-templated Ta-52 at.%Nb alloy generates entirely amorphous mixed-oxide films. These findings, complemented by the anodizing behavior and SEM examination results, confirm the high quality of the 3D nanostructured alloy and anodic films and underline their potential for capacitor application.

The diffractograms of the flat Ta-52 at.%Nb alloy shown in Fig. 5c reveal the same composition and crystal structure of the deposit and amorphous structure of the anodic film. The difference, however, is that, on a flat substrate, the Ta-52 at.%Nb crystallites grow substantially larger (~26 nm) and noticeably more oriented in [110] direction (perpendicular to the substrate) compared with the PAA-templated nanostructured coating. The later text will discuss the dissimilarities of anodic-film growth on the two types of Ta-52 at.%Nb coatings.

### 3.5. Electrical/dielectric properties of anodic films

The following flat and 3D anodic films were examined by EIS: (a) the as-anodized 50-V films (Fig. 6), (2) the 50-V films annealed at temperatures 100–300 °C (Fig. 7), (3) anodic films formed at anodizing voltages ranging 5 to 130 V before and after air-annealing at 200 °C (Fig. 9). Moreover, bias-dependent measurements were performed for the 50-V as-anodized and annealed anodic films (Fig. 8).

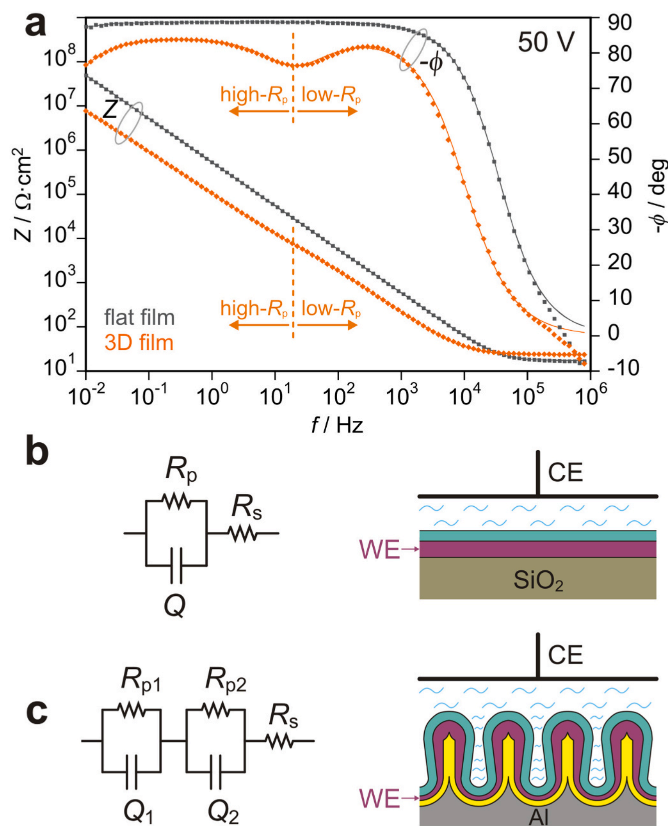


**Fig. 6.** (a) Experimental (symbols) and fitted (solid lines) Bode plots for the flat and 3D Ta-52 at.%Nb alloy films anodized to 50 V measured at 0 V. The double-layered behavior is seen in the Bode plot of the 3D nanofilm. (b, c) Equivalent electrical circuits adopted for fitting the Bode plots of the (b) flat and (c) 3D anodic films on Ta-52 at.%Nb alloys, together with schematic drawings showing the layer arrangement.

### 3.5.1. *Initial comparison*

Fig. 6a shows the Bode plots for the flat and 3D anodic films on the Ta-52 at.%Nb alloys anodized to 50 V. A linear decrease in the modulus of impedance, $Z$, with increasing frequency, $f$, at a slope of −1, while the phase shift, $\phi$, approaches −90°, in a broad frequency domain of 0.01–1000 Hz is noted for the flat film. The behavior can be fitted with a simple equivalent circuit containing a constant phase element (CPE), a parallel electrical resistance of the anodic film, $R_p$, and the electrical resistance of the electrolyte, $R_s$, in series with CPE and $R_p$ (Fig. 6b). The extracted from the CPE parameters capacitance $C = 0.332$ μF cm$^{-2}$.

In contrast, the 3D nanofilm anodized to the same 50 V is characterized by two time-constant distributions manifested by two well-distinguished features in the $-\phi$ vs $f$ plot. This Bode plot is fitted with two CPEs in series, each in parallel with a resistance (Fig. 6c). Such a circuit implies that the anodic film comprises two capacitive layers with substantially different $R_p$, further referred to as the 'low-$R_p$' and 'high-$R_p$' layers, associated with the high- and low-frequency domains, as pointed out in Fig. 6a. For the 50-V 3D anodic film, the values for $C$ extracted from the CPE parameters for the high-$R_p$ and low-$R_p$ layers are 2.23 and 3.40 μF·cm$^{-2}$, respectively (Fig. 6a). Under the assumption of a uniform dielectric constant $\varepsilon = 33$ and a ratio of the effective and apparent surface areas $A_e$:$A_a$ = 3.4 (both parameters will be justified later in the text) and based on the EIS measurements, we calculated the thickness, $d$, of the high-$R_p$ layer (∼45 nm) and the low-$R_p$ layer (∼29 nm) – in total ∼74 nm. For the 50-V flat anodic film, the calculated value for $d$ = ∼88 nm. Thus, the low-$R_p$ layer constitutes a considerable part of the anodic film. Further, the resistivities $\rho = R_{p,e}/d$ are calculated for the high-$R_p$ and low-$R_p$ layers, where $R_{p,e}$ stands for the value of $R_p$ for the effective surface area from the fitted Bode plots in Fig. 6a obtained by multiplying $R_p$ by the $A_e$:$A_a$ ratio. For the 50-V 3D nanofilm, the value for $\rho = 4$ MΩ cm$^2$ nm$^{-1}$ of the high-$R_p$ layer is incomparably higher than $\rho = 0.2$ kΩ cm$^2$ nm$^{-1}$ of the low-$R_p$ layer. For the 50-V flat anodic film, the high value for $\rho = 18$ MΩ cm$^2$ nm$^{-1}$ corresponds to the usual resistivities of anodic films on Ta and Nb, which behave as wide bandgap semiconductors or dielectrics [41]. Notably, the phase shift for the 50-V 3D nanofilm is much lower than for the 50-V flat anodic film (Fig. 6a), indicating relatively worse dielectric properties of the 3D nanofilm.

Such a double-layered behavior of the 50-V 3D nanofilm appeared to be unique to its flat counterpart examined here (Fig. 6a). The unusual behavior of the 3D nanofilm requires further investigation. In the following, we will show how the values for $C$ and $d$ depend upon the anodizing voltage and post-anodizing annealing.

### 3.5.2. *Impact of annealing*

Fig. 7a shows the Bode plots for the 50-V flat anodic film recorded after annealing in air at temperatures $T$ = 100–300 °C. All the plots are well fitted with a simple equivalent electrical circuit containing a single CPE shown in Fig. 6b. Typically, the $Z$-value decreases with increasing $T$ because of increasing $C$ (Fig. 7c). The $C$-value increases from 0.33 μF cm$^{-2}$ to 0.86 μF cm$^{-2}$ after annealing at $T$ = 300 °C. Assuming a uniform value for $\varepsilon = 33$, the value for $d$ calculated from the EIS measurements (Fig. 7d) decreases from 90 to 34 nm. Notably, a similar rise in the capacitance due to decreasing the EIS-determined value for $d$ after annealing was observed for anodic oxides formed at 50 V on thin Ta and Nb metallic layers. The reported effect of low-temperature air annealing on the properties of anodic niobium and tantalum oxides has been explained either by the formation of microcracks and other physical defects caused by the heating [42,43] or by oxygen diffusion into the films altering the film semiconducting properties and increasing leakage currents [44,45]. Since no physical defects were observed in the air-annealed anodic films prepared in the present study, we assume that changes in the film semiconducting properties account for the reduced EIS-measured film thickness and increased capacitance.

Fig. 7b shows the Bode plots for the 50-V 3D nanofilms after annealing up to 250 °C. The two-time-constant behavior becomes less pronounced with increasing $T$, fully vanishing after $T > 200$ °C. With increasing $T$, the lower-frequency values for $Z$ shift upward, whereas the higher-frequency values for $Z$ scarcely change. An equivalent circuit with two CPEs (Fig. 6c) is used for fitting, resulting in two values for $C$ corresponding to the high-$R_p$ and low-$R_p$ layers (Fig. 7c). The $C$-value of the high-$R_p$ layer decreases from 2.23 to 1.13 μF cm$^{-2}$ while the $C$-value for the low-$R_p$ layer increases from 3.4 up to 29.1 μF cm$^{-2}$. However, the sum of the two capacitances, proportional to the total film thickness determined by EIS, remains almost unchanged (∼1.2 μF cm$^{-2}$). Again, under the assumption of $\varepsilon = 33$ and $A_e$:$A_a$ ratio = 3.4, the high-$R_p$ layer thickens from 45 to 88 nm at $T$ = 250 °C while the low-$R_p$ layer thins from 29 to 3 nm at $T$ = 200 °C and becomes unidentified after annealing at $T$ = 250 °C (Fig. 7d). The total value for $d$ remains almost constant. After annealing at $T > 200$ °C, the film is composed of the high-$R_p$ layer only. The evolution of the layered film structure with increasing annealing temperature is shown in the schematic cross sections in Fig. 7f. One may see that the electrical behavior of the 3D nanofilm contrasts considerably with the flat anodic film (Fig. 7a).

The resistivities of the high-$R_p$ and low-$R_p$ layers for the 3D nanofilms with increasing $T$ are shown in Fig. 7e and compared with the flat anodic film. One may see that the high values for $\rho$ of the high-$R_p$ layer in the 3D nanofilm (∼3 to ∼20 MΩ cm$^2$ nm$^{-1}$) are comparable to the resistivities of the flat film (5–30 MΩ cm$^2$ nm$^{-1}$). The $\rho$-values for the low-$R_p$ layer are matchlessly smaller in the entire temperature range (0.1–0.5 kΩ cm$^2$ nm$^{-1}$). The $n$-value extracted from the CPE characteristics for the high-$R_p$ layers of the 50-V 3D nanofilm reveals a steady growth from 0.94 to 0.98 with increasing $T$ (inset in Fig. 7e). In contrast, the $n$-value for the 50-V flat anodic film steadily deteriorates from 0.99 to 0.97 in the same temperature range. This means that, with increasing annealing temperature, the dielectric properties of the flat film worsen, whereas

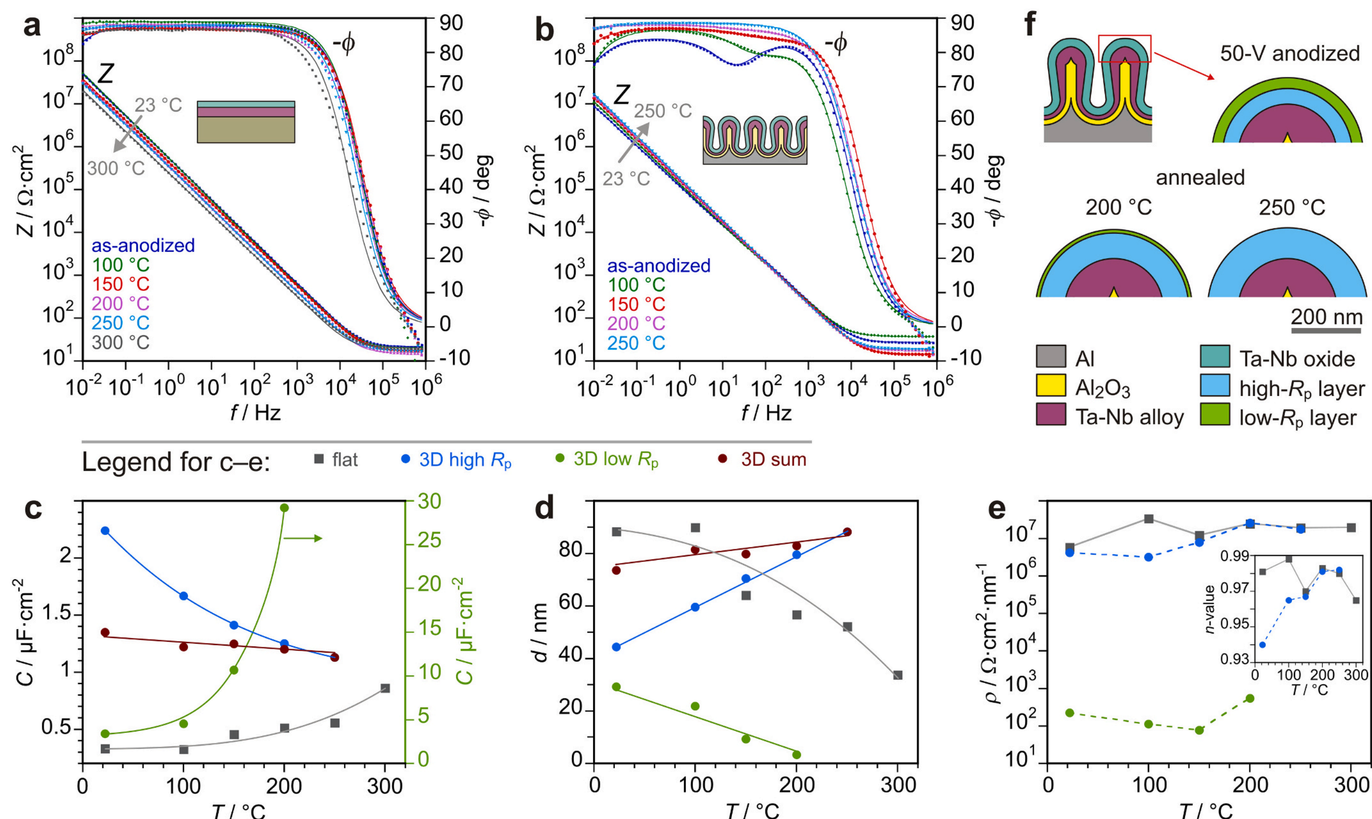


**Fig. 7.** (a, b) Experimental (symbols) and fitted (solid lines) Bode plots of the flat and 3D Ta-52 at.%Nb alloy films anodized to 50 V measured at 0 V before and after annealing at various temperatures. (c, d) Temperature dependences of capacitances, $C$, and thicknesses, $d$, derived from the Bode plots for the flat and 3D anodic films as a function of annealing temperature, $T$. (e) Resistivity, $\rho$ ($R_{p,e}/d$) vs. $T$ for the high-$R_p$ and low-$R_p$ layers in the 3D anodic nanofilm. The inset in (e) shows the annealing-temperature dependence of $n$-values for the two film types. (f) Schematics showing the evolution of the high-$R_p$ (blue) and low-$R_p$ (green) layers in the 3D anodic films with air annealing.

the two-layered structure of the 3D nanofilm gradually transforms into a single high-$R_p$ layer (at $T > 200$ °C), which then behaves almost like an ideal dielectric.

In summary, the double-layered behavior of the 3D nanofilms flattens with air annealing, reaching a state where only the high-$R_p$ layer is present. The total capacitance of the 3D nanofilm scarcely changes with annealing temperature, contrarily to the temperature-dependent flat anodic films. Furthermore, the high-$R_p$ layer of the 3D nanofilm becomes increasingly dielectric after annealing, the $n$-value exceeding those of the flat film. From the practical viewpoint, the 3D air-annealed anodic film overperforms its flat counterpart. Together with the up to 4.5 times increased capacitance density, the electrical characteristics of the 3D nanofilms are advantageous for their potential application in electrolytic capacitors.

### 3.5.3. Mott-Schottky analysis

Oxides grown anodically on pure Nb are frequently $n$-type semiconductors [42,43,45], whereas anodic oxides on pure Ta often behave more like dielectrics [39,45,46]. Several studies by Habazaki and coworkers performed on 50-V anodic films on Nb alloyed with N or Si have shown that already small amounts of the foreign elements may cause the transformation from semiconducting to dielectric behavior of the anodic films [42,43]. On the other hand, relatively thinner 3-V anodic films on Ta-Nb alloy layers having 5–95 at.% of Nb revealed semiconducting properties in the whole concentration range [18]. The diversity and sometimes contradiction of the reported experimental results and the unusual behavior of the films prepared here motivated us to explore the nature of the mixed Ta-52 at.%Nb oxides in depth via Mott-Schottky measurements. The 50-V 3D nanofilms were chosen as a model system for such an analysis and compared with the 50-V flat anodic films.

The measured and fitted Bode plots obtained for the *flat* anodic films are shown in Fig. 8a. A simple equivalent circuit comprising one CPE in parallel with $R_p$ (shown in the inset of Fig. 8a) is used to fit the experimental plots. The value for $C$ extracted from the CPE parameters, that is, a single value for capacitance for the whole frequency range, decreases from 0.342 µF cm$^{-2}$ at −1.0 V to 0.283 µF cm$^{-2}$ at 5.0 V (not shown), resulting in a slight rise in $1/C^2$ with $U_b$ (Mott-Schottky plot in Fig. 8d, grey symbols). The behavior is typical for $n$-type semiconductors with low donor concentrations, $N_d$. Thus, assuming $\varepsilon = 33$ and using the grey-line slope in Fig. 8d, the calculated value for $N_d = 2.8 \times 10^{18}$ cm$^{-3}$, which is comparable to $N_d$ in a thick anodic oxide grown on pure Nb ($1 \times 10^{18}$ cm$^{-3}$) [42,43], and it is 10-fold smaller than $N_d$ determined for thin anodic oxides on Ta-Nb alloys reported in previous work [18].

In the following, we will describe the method to estimate the value for $\varepsilon$ of the mixed-oxide anodic films prepared in this study. Assuming that the 50-V flat anodic film has a uniform dielectric constant and an even thickness of 100 nm (measured by SEM), the Mott-Schottky measurements revealed that $C$ decays to a constant value of 0.289 ± 0.006 µF·cm$^{-2}$ when $U_b$ is raised above 2.0 V, above which the anodic film becomes fully depleted. From these data, the calculated value for $\varepsilon = 33$. This value fits precisely the average $\varepsilon$-value reported for pure $Ta_2O_5$ (27) [39,45] and pure $Nb_2O_5$ (~40) [39,42,43,45]. The Impact of the thin $Nb_2O_5$ anodic film at the film/electrolyte interface (disclosed by XPS) may be neglected because it is incomparably thin (a few nanometers) and superimposed (connected in series) with the Ta-Nb mixed-oxide layer of the dominating thickness (~100 nm). Considering the amorphous nature of the flat and structured anodic films and neglecting the differences in their chemical compositions, the same value for $\varepsilon$ is adopted for calculating $d$-values for the 3D nanofilms prepared in this

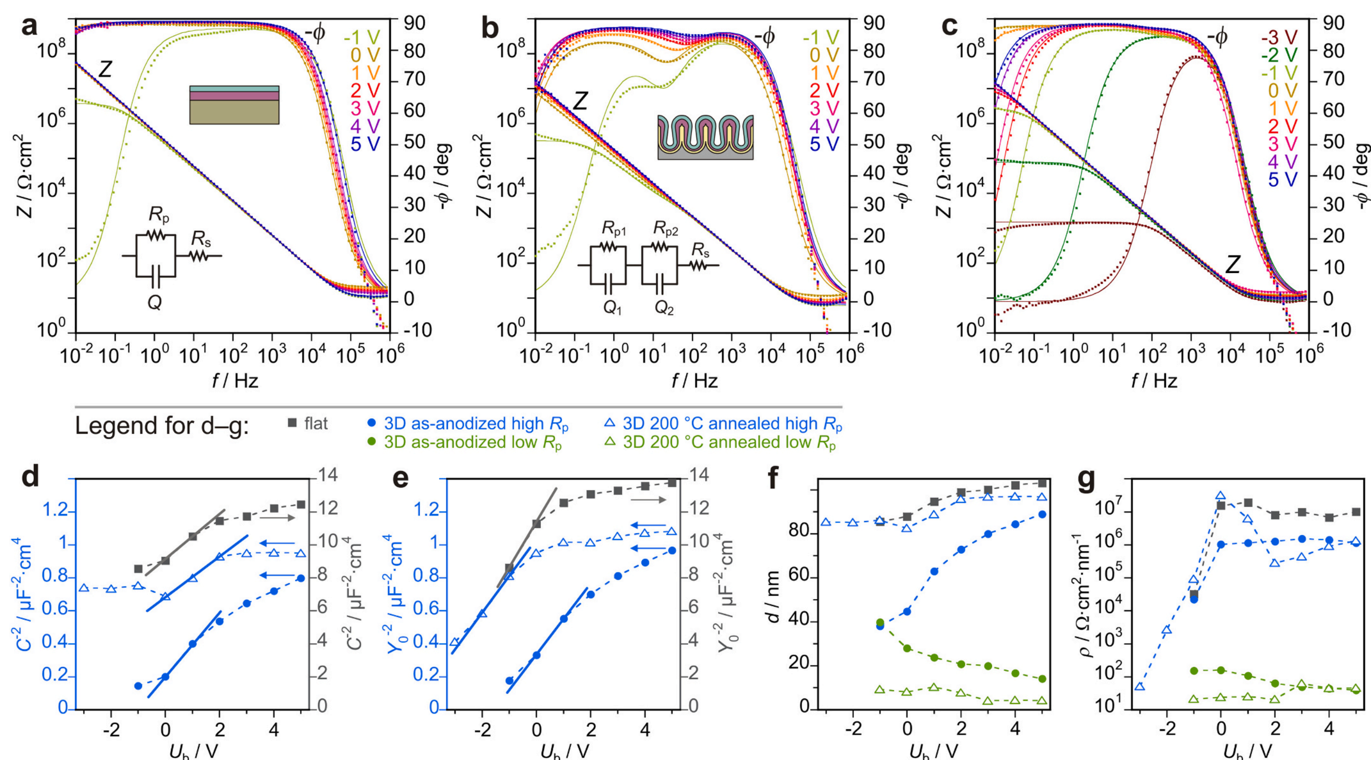


**Fig. 8.** Experimental (symbols) and fitted (solid lines) Bode plots of the (a) as-anodized flat anodic film, (b) as-anodized 3D anodic film, and (c) 200 °C-annealed 3D anodic film measured at various bias potentials, $U_b$. (d) Mott-Schottky, (e) $1/Y_0^2$ vs. $U_b$, (f) $d$ vs. $U_b$, and (g) $\rho$ vs. $U_b$ plots of the as-anodized flat anodic film, as-anodized 3D anodic film, and 200 °C-heated 3D anodic film calculated from the Bode plots in (a), (b), and (c), respectively. Only the high-$R_p$ layers were considered in (d) and (e). All anodic films were formed by anodizing to 50 V.

study.

Due to the well-pronounced two-layer behavior of the 3D nanofilm anodized to 50 V (Fig. 8b), which becomes less evident with increasing $U_b$, the data were fit using a two-CPE equivalent circuit (inset in Fig. 8b). The capacitance of the high-$R_p$ layer decreases from 2.6 μF cm$^{-2}$ at −1.0 V to 1.1 μF cm$^{-2}$ at 5.0 V, whereas the capacitance of the low-$R_p$ layer increases linearly from 2.5 μF cm$^{-2}$ at −1.0 V to 7.0 μF cm$^{-2}$ at 5.0 V (not shown). Assuming that most of the bias potential drops on the high-$R_p$ layer, the change in the high-$R_p$ layer capacitance is due to the change in the depletion layer that forms within the high-$R_p$ layer. Therefore, the value for $N_d = 1.8 \times 10^{18}$ cm$^{-3}$ calculated from the Mott-Schottky plot made for the high-$R_p$ layer capacitance (Fig. 8d, blue circles, assuming $\varepsilon = 33$ and $A_e$:$A_a = 3.4$) ascribes the 3D nanofilm as a lightly-doped $n$-type semiconductor, similarly to the flat anodic oxide.

Mott-Schottky measurements of the 50-V 3D nanofilm after annealing at $T = 200$ °C (Fig. 8c) were performed and evaluated following the described above procedure. Contrarily to the previous two cases, here the high-$R_p$ layer capacitance remains unchanged between −3.0 and 0.0 V (1.17 ± 0.02 μF cm$^{-2}$) and slightly decreases to 1.025 μF cm$^{-2}$ at 5.0 V only (not shown). This is reflected by the high-placed plateau at potentials below 0.0 V in Fig. 8d (blue triangles), which is probably caused by the small parallel resistance at cathodic potentials [37]. Therefore, the admittance, $Y_0$, extracted from the CPE parameters was used to modify the Mott-Schottky plots (Fig. 8e), resulting in more apparent trends reinforcing the conclusion on the $n$-type semiconducting behavior [37]. Thus, $N_d = 2.4 \times 10^{18}$ cm$^{-3}$ is calculated from the $1/C^2$ vs. $U_b$ plot, while $N_d = 1.7 \times 10^{18}$ cm$^{-3}$ is calculated from the $1/Y_0^2$ vs. $U_b$ plot. It should be noted that the $1/Y_0^2$ vs. $U_b$ plots give the same $N_d = 1.6 \times 10^{18}$ cm$^{-3}$ for both the flat and 3D anodic films.

Changes in $d$-values with $U_b$ are shown in Fig. 8f. The thickness of the 50-V flat film increases from 85 to 102 nm, meaning that the depletion layer thickens with increasing $U_b$. Similarly, the high-$R_p$ layers of the as-anodized 3D nanofilm and the 200 °C-annealed 3D film thicken with increasing $U_b$. On the other hand, the low-$R_p$ layers become thinner with increasing $U_b$. Notably, when measured at 0.0 V, the total $d$ = ~74 nm for the as-anodized 3D film, while $d$ = ~88 nm for the flat film. The discrepancy arises due to the dissimilar semiconducting properties of the two films. In addition, considering that, in the 50-V 3D nanofilm, the low-$R_p$ layer is superimposed on the high-$R_p$ layer, the sum of their thicknesses obtained at $U_b > 3.0$ V (when the entire high-$R_p$ layer is depleted) and the apparent $\varepsilon$ are comparable to those of the 50-V flat film, the ratio of $C$ = 0.982 μF cm$^{-2}$ for the structured film and $C$ = 0.287 μF cm$^{-2}$ for the flat film (both calculated at $U_b > 3.0$ V) should be equal to the ratio of the effective and apparent surface areas $A_e$:$A_a$ = 3.4 associated with the 3D nanofilm.

Considering the electrical properties of the layers in the 3D anodic films (Fig. 8g), one may see that the $\rho$-values for both the flat film and the high-$R_p$ layers in the 3D film lie in the MΩ cm$^2$ nm$^{-1}$ range when measured at bias potentials above 0 V. The range widens in the Mott-Schotky measurements (0.3–30 MΩ cm$^2$ nm$^{-1}$). Below −1.0 V, the $\rho$-value decreases gradually to a level typical for the low-$R_p$ layers (30–160 Ω cm$^2$ nm$^{-1}$).

Although the best $n$-values are extracted from the CPE parameters for the flat film (improving from 0.98 at −1.0 V to 0.99 at >2.0 V, not shown), the 200 °C annealed 3D nanofilm shows competitive $n$-values (0.98) at $U_b > 0$ V. Relatively worse $n$-values are attributed to the as-anodized (thermally untreated) nanostructured film, increasing from 0.90 at −1.0 V to 0.97 at >3.0 V.

In summary, the Mott-Schottky measurements revealed that the flat and 3D nanofilms are $n$-type semiconductors with low donor densities $N_d$ = ~$2 \times 10^{18}$ cm$^{-3}$. This finding implies that the alloying of Nb with 48 at.% Ta is insufficient for the transition from semiconductor to fully dielectric properties of anodic oxide on the alloy, regardless of the supporting substrates. The featured double-layered behavior of the as-anodized 3D film becomes less pronounced at higher bias potentials due to the thinning of the low-$R_p$ layer. The low-temperature post-

anodizing air-annealing of the 3D nanofilm enhances the effect even further.

*3.5.4. Stepwise Ta-Nb alloy anodizing*

To disclose the origin and understand the electrical behavior of the low-$R_p$ layer in the 3D nanofilms, the PAA-templated alloy was anodized from 10 to 130 V in 10 V steps. After each anodizing step, the film was examined by EIS at 0.0 V. To explore the effect of annealing, after each anodizing step followed by recording EIS diagram, the film was annealed at 200 °C for 1 h and analyzed by EIS at 0.0 V again. The experimental and fitted Bode plots for the stepwise anodized and annealed 3D nanofilms are shown in Fig. 9a–c. The analysis of the experimental data is presented in Fig. 9d–g.

The Bode plots of the as-anodized 3D nanofilms (Fig. 9a) show a pronounced double-layered behavior beginning from $U_a = 40$ V, whereas a single-layer behavior is noted for $U_a \leq 30$ V. This implies that the low-$R_p$ layer starts to form only at $U_a \geq 30$ V. Annealing the films after each anodizing step (Fig. 9b) results in substantially flattening the double-layer behavior. Moreover, the phase shift improves with increasing $U_a$ above 30 V. A comparison of the selected Bode plots before and after the annealing is shown in Fig. 9c. Interestingly, the *Z*-value of the 30-V 3D nanofilm does not change much after the annealing in the entire frequency range, whereas for the 80- and 130-V films, the *Z*-value at frequencies below ~10 Hz rises substantially. The Bode plots were fitted accordingly – using an equivalent circuit involving one or two CPEs, each in parallel with $R_p$.

The calculated values for $C$ decrease with increasing $U_a$ (not shown), as can be expected due to the thickening of the layers with anodizing voltage. The flat anodic films show a single capacitance with a linear increase in $1/C$ vs. $U_a$ (Fig. 9d, grey symbols), meaning a linear rise in $d$ with $U_a$ (Fig. 9f), as expected from the high-field growth kinetics [47]. For the reasons explained below, the $1/C$ vs. $U_a$ data associated with the nanostructured films cannot be linearly fitted with a constant slope in the entire voltage range.

## 4. Discussion

Until now, there have been no reports on forming a smooth continuous metal or metal-alloy conducting layer in the alumina nanopores. Masuda and Satoh [48] have utilized a very thin PAA template for forming an array of Au nanodots on a substrate via electron-beam vacuum evaporation. Although K. Yasui and co-workers have succeeded in filling the alumina nanopores with metal by vacuum deposition, no space was left in the pores free from the deposit [49]. Yong-il Park and co-workers have reported the formation of Y-Zr metal deposits onto PAA templates with pore sizes of 20 and 200 nm using a DC magnetron sputtering method. However, the deposited metal covered the pore necks and PAA surface only, blocking the pore outlets before any coverage was made inside the pores [50]. The success of our work is explained by experimentally disclosing the right combination of the technological, electrical, and electrolytic conditions for fabricating a PAA template with the most appropriate relation between the pore size, pore depth, and interpore spacing, enabling the sputtered atoms to enter the pores and condense on the pore walls most evenly and without interruptions.

The $A_e$:$A_a$ ratio is expected to vary with $U_a$ due to specific features of the PAA substrate and the unevenness in the stepwise thickening of the various parts of the anodic films. The $A_e$:$A_a$ ratio was calculated, as described above, at 0 V, neglecting the impact of the film's semiconducting nature for each anodizing voltage (Fig. 9e). The uneven behavior of the $A_e$:$A_a$ ratio with increasing $U_a$ is associated with the following overlapping effects:

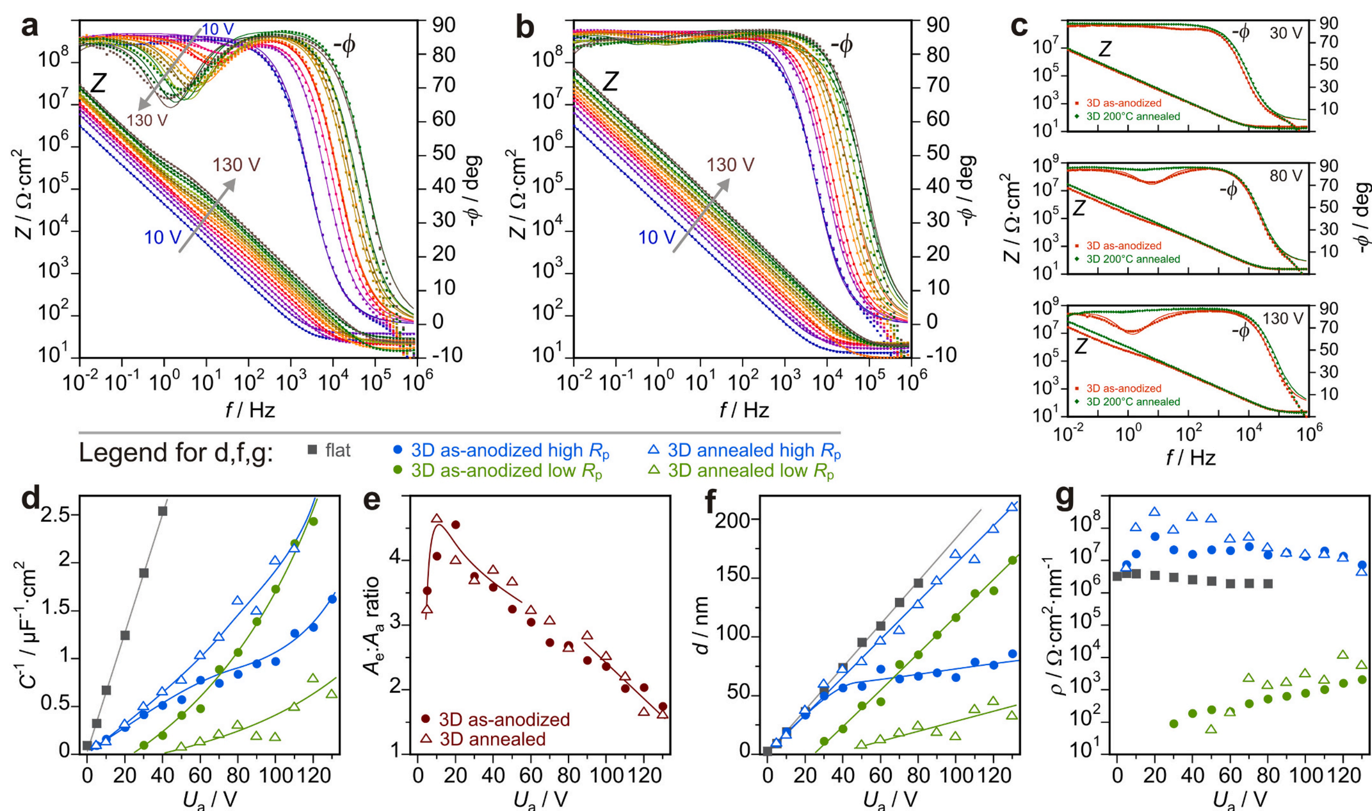


**Fig. 9.** Upper row: Experimental (symbols) and fitted (solid lines) Bode plots of the 3D anodic films (a) stepwise anodized from 10 to 130 V, (b) stepwise anodized and annealed after each anodizing step at 200 °C. Selected plots are shown individually in (c). Lower panel: comparative (d) reciprocal capacitance, (e) effective-to-apparent surface ratio, $A_e$:$A_a$, (f) EIS-determined film thickness, and (g) resistivity of the 3D and flat anodic films.

(1) At the low anodizing voltages, the initial surface nanomorphology of the deposited alloy is preserved over the entire film surface, which contributes to enlarging the effective surface area at the electrolyte/film interface in addition to the PAA-templated structure of the deposit. Simultaneously, the film/metal interface expands due to the consumption of the deposited alloy. These effects account for the initial surge in the $A_e$:$A_a$ ratio up to 4.5 at $U_a$ = 5–20 V.
(2) With the thickening of the anodic film, the porosity at the electrolyte/film interface becomes lower due to the narrowing of the pores owing to the volume expansion of growing oxide. The nanomorphology of the anodic film is no longer preserved at $U_a$ > 30 V. The two effects largely account for the decay of the $A_e$:$A_a$ ratio to ~3.5 at $U_a$ = 30–60 V.
(3) With further anodizing, the remaining alloy continues to thin and, at a certain voltage, becomes fully consumed locally inside the pores where the deposit is the thinnest (~55 nm) – on the pore walls and bottoms, as shown schematically in Fig. 10a. Under the assumption of the film formation ratio of 2.0 nm $V^{-1}$ and Pilling-Bedworth ratio of 2.5 [19,51], the thinnest parts of the alloy film should be fully oxidized at $U_a$ = ~70 V. The area of the consumed alloy extends continuously with increasing $U_a$, shrinking the surface of the bottom electrode and continuously making $A_e$ smaller, as depicted in Fig. 10b. Likely, the entire consumption of the alloy at the pore walls and bottoms accounts for the change in the $A_e$:$A_a$ vs. $U_a$ slope in the range of ~60 to 80 V.
(4) The oxide grown over the pore necks and the interpore peaks swallows and flattens continuously with anodizing voltage until it blocks the pore necks, preventing the bulk electrolyte from entering the pores (Fig. 10b). Because of the not very narrow pore-size distribution and some thickness inhomogeneity in the deposited alloy across the sample surface, the two phenomena evolve gradually, resulting in systematically reducing the $A_e$:$A_a$ ratio from ~2.5 to ~1.5 at $U_a$ = 80–130 V. The pore necks become hardly identified, and the film grows almost as a flat layer with an increase in $U_a$ over 150 V, as shown in the SEM image in Fig. S9.

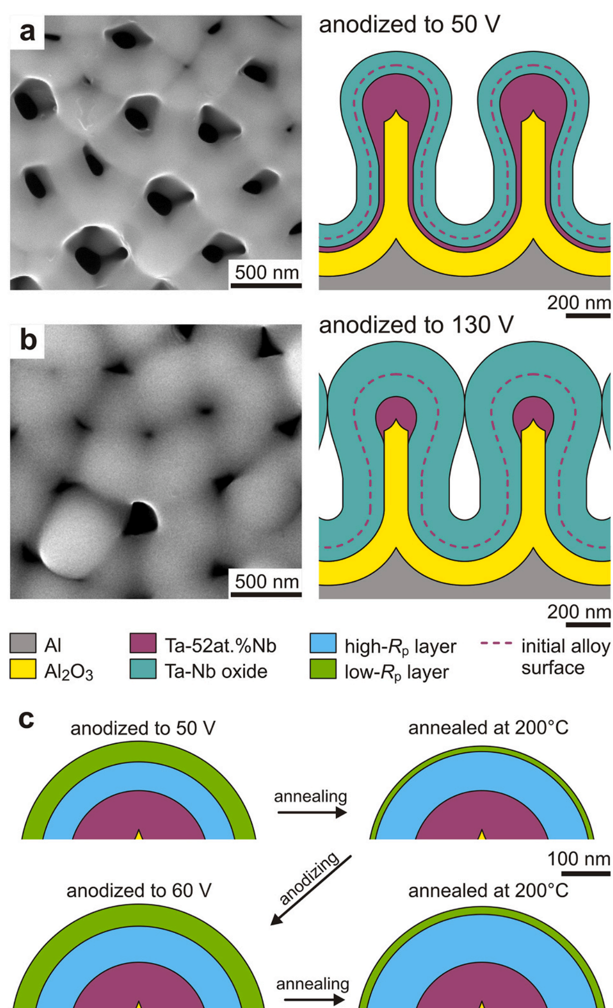


**Fig. 10.** (a, b) Surface-view SEM images and schematics of corresponding cross-sections of a 3D Ta-52 at.%Nb alloy anodized to (a) 50 V and (b) 130 V. (c) Schematic views explaining the impact of annealing and repeated anodizing on the thicknesses of the high-$R_p$ and low-$R_p$ layers in the 3D Ta-52 at.%Nb alloy films anodized to 50 V and then 60 V.

Using the estimated $A_e$:$A_a$ ratio for each value for anodizing voltage, the thicknesses of the various layers in the 3D nanofilms may be calculated based on the $C$-values extracted from the CPE parameters (Fig. 9f). The experimental $d$ vs. $U_a$ curve for the flat film is added for comparison. The high-$R_p$ layer thickness increases linearly up to 30 V, similar to the flat film. Beyond ~40 V, the rate begins to retard. From this point, the low-$R_p$ layer begins to form, thickening proportionally to anodizing voltage, dominating in the pair and occupying 50 to 70 % of the total film thickness with increasing $U_a$ from 70 to 130 V. For the stepwise anodized and then annealed at 200 °C 3D films, a linear thickening of the high-$R_p$ layer is observed with increasing $U_a$. The impact of the annealing that makes the high-$R_p$ layer dominate and finally take the entire film depth is exceptionally favorable for applying these films as capacitor dielectrics.

The state when the low-$R_p$ layer partially (or fully) transforms into the high-$R_p$ layer due to the annealing is preserved unless the film is anodized to the same or higher voltage again. Another annealing restores the high-$R_p$ state. For example, Fig. 10c depicts such transitions in the two-layered structure of a film that was first anodized to 50 V, then annealed at 200 °C, then anodized to 60 V, and annealed at 200 °C afterward.

The values for $\rho$ of the high-$R_p$ layers remain in the order of ~10–100 MΩ $cm^2$ $nm^{-1}$, increasing after the 200 °C annealing by order of magnitude in the voltage range of 10–50 V (Fig. 9g). In this regard, the 3D nanofilms overperform their flat counterparts ($\rho$ < 5 MΩ $cm^2$ $nm^{-1}$) and anodic films on Ta or Nb [39,41].

The impact of annealing on the low-$R_p$ layer in the 3D nanofilms cannot be explained by chemical or structural changes because, at such relatively low annealing temperatures, crystallization of the oxide material or recrystallization of the remaining alloy does not occur. Thermal oxidation or oxygen diffusion out of the oxide is not expected, nor do physical defects form in the oxide, as revealed by SEM examination. Instead, we assume that the formation of an immobile negative space charge [52] in the outer layer of the freshly prepared 3D oxide films accounts for the two-layered electrical behavior. According to previous reports [53,54], during anodizing, the field-induced ionization of the water molecules yields electrons, protons, and free radicals (OH•). The released electrons create a 'virtual' cathode, which can, under a particular field, eject electrons into the growing anodic film [54]. The ejected electrons are captured by the trapping centers in the film, such as incorporated electrolyte-derived species or oxygen vacancies energetically localized near the conduction band. Filling the electron traps with electrons creates a negative space charge in the outer part of the film material. The depth of the space-charge layer and its uniformity may depend on the anodizing voltage, the local field distribution, and the presence and distribution of impurities and substoichiometric oxides (positively charged oxygen vacancies) in the film. For $U_a$ < 30 V, a space charge does not form because the effect seems to be voltage- or field-strength-dependent, as revealed in the case of anodic oxide films on aluminum [55]. The process of filling the traps depends on the

temperature. The emission of electrons from the trap states to the conduction band is activated by annealing, and the space charge is reduced or completely disappears depending on the annealing temperature and time.

The presence of a space charge in the 3D nanofilms and its absence in the flat films can be explained based on the compositional and structural differences in the two film types. Both films grow on the Ta-52 at.%Nb alloy by migration of cations and anions, with slower migration of $Ta^{5+}$ ions relative to $Nb^{5+}$ ions. This leads to unevenly mixing the two oxides across the film depth, forming a niobium-oxide-rich outer film layer, which is relatively thinner in the 3D nanofilm. The migration rates of $Ta^{5+}$ and $Nb^{5+}$ ions may differ in the flat and structured anodic films, resulting in a different Ta:Nb ratio in the two films. The concurrent migration of cations of lower oxidation states such as $Ta^{4+}$, $Ta^{3+}$, $Nb^{4+}$, and $Nb^{3+}$ at competitive to $Ta^{5+}$ and $Nb^{5+}$ rates occurs exclusively in the nanostructured anodic film, as was previously revealed for the case of the PAA-assisted anodization of Ta [56], resulting in the formation of a considerable amount of corresponding suboxides in addition to oxygen-deficient pentoxide in the 3D film composition.

In contrast, anodic oxides on the flat alloy contain fully stoichiometric $Ta_2O_5$ and $Nb_2O_5$ units. The unusually low-binding-energy O 1s and O 2s peaks in the XP spectra of the 3D nanofilm denote the presence of additional extraordinary compositional features in the 3D anodic films with no counterparts in the flat oxides. More compositional dissimilarities in the two film types potentially impacting their electronic properties may be expected due to the differences in the size and orientation of nanocrystallites and film grains in the Ta-52 at.%Nb solid solutions coated on the two substrates.

## 5. Summary and conclusions

The following conclusions can be drawn from the present study.

1. The Ta-52 at.%Nb alloy coatings were magnetron sputter-deposited and partially anodized over a PAA template with 500 nm pores to form high-quality continuous 3D alloy/oxide nanofilms of up to 4.5 times enlarged surface area.
2. The anodic films grow by migration of cations and anions, with slower migration of $Ta^{5+}$ ions relative to $Nb^{5+}$ ions, creating mixed oxides in the film depth. The unusual migration of $Ta^{4+}$, $Ta^{3+}$, $Nb^{4+}$, and $Nb^{3+}$ ions forms several suboxides in the 3D anodic-oxide nanofilm.
3. The anodic films behave as an *n*-type semiconductor with low donor densities $N_d = \sim 2 \times 10^{18}$ cm$^{-3}$, appropriate for dielectric applications.
4. The two-layered structure revealed for the 3D nanofilms anodized above 30 V transforms into a single high-resistivity (~100 MΩ cm$^2$ nm$^{-1}$) layer after air annealing at temperatures over 200 °C due to releasing the negative space charge from the outer film part.
5. The capacitance of the 3D oxide nanofilm formed by anodizing to practical 50 V is 1.2 μF cm$^{-2}$ and independent of annealing temperature, while the anodic oxide becomes increasingly dielectric with rising annealing temperature above 200 °C.
6. The coatings developed here may be utilized as novel 3D nanostructured electrodes/dielectrics for electrolytic microcapacitors suitable for traditional electronic circuits and energy-storage applications. Gas-sensing, superhydrophobic, or biomedical effects may also arise in these 3D nanofilms, similar to some previously reported self-organized anodic oxides on valve metals [26,57–59].

## CRediT authorship contribution statement

**Alexander Mozalev:** Writing – review & editing, Writing – original draft, Visualization, Resources, Project administration, Methodology, Investigation, Funding acquisition, Conceptualization. **Maria Bendova:** Writing – original draft, Visualization, Validation, Methodology, Investigation, Formal analysis, Data curation. **Francesc Gispert-Guirado:** Validation, Investigation, Formal analysis, Data curation. **Eduard Llobet:** Writing – review & editing, Supervision, Resources, Funding acquisition. **Hiroki Habazaki:** Writing – review & editing, Supervision, Resources.

## Declaration of competing interest

The authors declare that they have no known competing financial interests or personal relationships that could have appeared to influence the work reported in this paper.

## Data availability

Data will be made available on request.

## Acknowledgments

This research was supported by the Czech Science Foundation (GAČR) grant no. 20-25486S. CzechNanoLab project LM2018110 funded by MEYS ČR is acknowledged for financial support of recording XP spectra at CEITEC Nano Research Infrastructure. E.L. was supported by the Catalan Institution for Research and Advanced Studies via the 2023 Edition of the ICREA Academia Award, Catalonia, Spain.

## Appendix A. Supplementary data

Supplementary data to this article can be found online at https://doi.org/10.1016/j.surfcoat.2024.131042.

## References

[1] H. Zhao, Y. Lei, 3D nanostructures for the next generation of high-performance nanodevices for electrochemical energy conversion and storage, Adv. Energy Mater. 10 (2020) 2001460, https://doi.org/10.1002/aenm.202001460.
[2] P. Roy, S. Berger, P. Schmuki, $TiO_2$ nanotubes: synthesis and applications, Angew, Chem. Int. 50 (2011) 2904–2939, https://doi.org/10.1002/anie.201001374.
[3] D. Routkevitch, T. Bigioni, M. Moskovits, J.M. Xu, Electrochemical fabrication of CdS nanowire arrays in porous anodic aluminum oxide templates, J. Phys. Chem. 100 (1996) 14037–14047, https://doi.org/10.1021/jp952910m.
[4] W. Lee, S.J. Park, Porous anodic aluminum oxide: anodization and templated synthesis of functional nanostructures, Chem. Rev. 114 (2014) 7487–7556, https://doi.org/10.1021/cr500002z.
[5] K.B. Shelimov, D.N. Davydov, M. Moskovits, Template-grown high-density nanocapacitor arrays, Appl. Phys. Lett. 77 (2000) 1722–1724, https://doi.org/10.1063/1.1290598.
[6] J.W. Elam, D. Routkevitch, P.P. Mardilovich, S.M. George, Conformal coating on ultrahigh-aspect-ratio nanopores of anodic alumina by atomic layer deposition, Chem. Mater. 15 (2003) 3507–3517, https://doi.org/10.1021/cm0303080.
[7] L. Wen, R. Xu, Y. Mi, Y. Lei, Multiple nanostructures based on anodized aluminium oxide templates, Nat. Nanotechnol. 12 (2017) 244–250, https://doi.org/10.1038/nnano.2016.257.
[8] F. Ali, K.-H. Kim, Three-dimensional electrostatic capacitors as futuristic miniaturized energy storage component for energy autonomous systems, Energy Storage 3 (2021) e225, https://doi.org/10.1002/est2.225.
[9] L.J. Fernández-Menéndez, A.S. González, V. Vega, V.M. De la Prida, Electrostatic supercapacitors by atomic layer deposition on nanoporous anodic alumina templates for environmentally sustainable energy storage, Coatings 8 (2018) 403, https://doi.org/10.3390/coatings8110403.
[10] L. Iglesias, V. Vega, J. García, B. Hernando, V.M. Prida, Development of electrostatic supercapacitors by atomic layer deposition on nanoporous anodic aluminum oxides for energy harvesting applications, Front. Phys. 3 (2015) 12, https://doi.org/10.3389/fphy.2015.00012.
[11] L.C. Haspert, S.B. Lee, G.W. Rubloff, Nanoengineering strategies for metal–insulator–metal electrostatic nanocapacitors, ACS Nano 6 (2012) 3528–3536, https://doi.org/10.1021/nn300553r.
[12] P. Banerjee, I. Perez, J. Henn-Hecordier, S.B. Lee, Nanotubular metal–insulator–metal capacitor arrays for energy storage, Nat. Nanotechnol. 4 (2009) 292–296, https://doi.org/10.1038/nnano.2009.37.
[13] L. Assaud, K. Pitzschel, M.K.S. Barr, M. Petit, G. Monier, M. Hanbücken, L. Santínaccí, Atomic layer deposition of $HfO_2$ for integration into three-dimensional metal–insulator–metal devices, Appl. Phys. A Mater. Sci. Process. 123 (2017) 768, https://doi.org/10.1007/s00339-017-1379-2.
[14] H. Liu, G. Zhang, X. Zheng, F. Chen, H. Duan, Emerging miniaturized energy storage devices for microsystem applications: from design to integration, Int. J. Extrem. Manuf. 2 (2020) 042001, https://doi.org/10.1088/2631-7990/abba12.

[15] S. Diblik, T. Zednicek, New technologies on tantalum and niobium oxide capacitors for space-limited designs, in: 2006 1st Electronic Systemintegration Technology Conference, IEEE, 2007, https://doi.org/10.1109/ESTC.2006.280104.
[16] F. Di Franco, G. Zampardi, M. Santamaria, F. Di Quarto, H. Habazaki, Characterization of the solid state properties of anodic oxides on magnetron sputtered Ta, Nb and Ta-Nb alloys, J. Electrochem. Soc. 159 (2012) C33–C39, https://doi.org/10.1149/2.031201jes.
[17] G. Tranchida, A. Zaffora, F. Di Franco, M. Santamaria, The effect of anodizing bath composition on the electronic properties of anodic Ta-Nb mixed oxides, Nanomaterials 12 (2022) 4439, https://doi.org/10.3390/nano12244439.
[18] A.I. Mardare, A. Ludqig, A. Savan, A.W. Hassel, Electrochemistry on binary valve metal combinatorial libraries: niobium-tantalum thin films, Electrochim. Acta 140 (2014) 366–375, https://doi.org/10.1016/j.electacta.2014.02.138.
[19] S. Komiyama, E. Tsuji, Y. Aokí, H. Habazaki, Growth and field crystallization of anodic films on Ta–Nb alloys, J. Solid State Electrochem. 16 (2012) 1595–1604, https://doi.org/10.1007/s10008-011-1565-7.
[20] C.S. Blackman, X. Correig, V. Katko, A. Mozalev, I.P. Parkin, R. Alcubilla, T. Trifonov, Templated growth of tungsten oxide micro/nanostructures using aerosol assisted chemical vapour deposition, Mater. Lett. 62 (2008) 4582–4584, https://doi.org/10.1016/j.matlet.2008.08.027.
[21] S. Ono, M. Saito, H. Asoh, Self-ordering of anodic porous alumina formed in organic acid electrolytes, Electrochem. Acta 51 (2005) 827–833, https://doi.org/10.1016/j.electacta.2005.05.058.
[22] A. Mozalev, A. Surganov, S. Magaino, Anodic process for forming nanostructured metal-oxide coatings for large-value precise microfilm resistor fabrication, Electrochim. Acta 44 (1999) 3891–3898, https://doi.org/10.1016/S0013-4686(99)00096-1.
[23] A. Mozalev, I. Mozaleva, M. Sakairi, H. Takahashi, Anodic film growth on Al layers and Ta–Al metal bilayers in citric acid electrolytes, Electrochim. Acta 50 (2005) 5065–5075, https://doi.org/10.1016/j.electacta.2005.02.092.
[24] S. Ono, M. Saito, M. Ishiguro, H. Asoh, Controlling factor of self-ordering of anodic porous alumina, J. Electrochem. Soc. 151 (2004) B473–B478, https://doi.org/10.1149/1.1767838.
[25] V. Surganov, P. Morgen, J.G. Nielsen, G. Gorokh, A. Mozalev, Study of the initial stage of aluminium anodization in malonic acid solution, Electrochem. Acta 32 (1987) 1125–1127, https://doi.org/10.1016/0013-4686(87)90043-0.
[26] Z. Pytlicek, M. Bendova, J. Prasek, A. Mozalev, On-chip sensor solution for hydrogen gas detection with the anodic niobium-oxide nanorod arrays, Sensors Actuators B Chem. 284 (2019) 723–735, https://doi.org/10.1016/j.snb.2019.01.009.
[27] A. Mozalev, M. Sakairi, H. Takahashi, Structure, morphology, and dielectric properties of nanocomposite oxide films formed by anodizing of sputter-deposited Ta-Al bilayers, J. Electrochem. Soc. 151 (2004) F257–F268, https://doi.org/10.1149/1.1796445.
[28] A. Mozalev, M. Bendova, R.M. Vazquez, Z. Pytlicek, E. Llobet, J. Hubalek, Formation and gas-sensing properties of a porous-alumina-assisted 3-D niobium-oxide nanofilm, Sensors Actuators B Chem. 229 (2016) 587–598, https://doi.org/10.1016/j.snb.2016.02.024.
[29] A. Mozalev, R.M. Vázquez, C. Bittencourt, D. Cossement, F. Gispert-Guirado, E. Llobet, H. Habazaki, Formation–structure–properties of niobium-oxide nanocolumn arrays via self-organized anodization of sputter-deposited aluminum-on-niobium layers, J. Mater. Chem. C 2 (2014) 4847–4860, https://doi.org/10.1039/c4tc00349g.
[30] A. Mozalev, M. Bendova, F. Gispert-Guirado, E. Llobet, Hafnium-oxide 3-D nanofilms via the anodizing of Al/Hf metal layers, Chem. Mater. 30 (2018) 2694–2708, https://doi.org/10.1021/acs.chemmater.8b00188.
[31] X-ray photoelectron spectroscopy (XPS) reference pages, Adventitious carbon. http://www.xpsfitting.com/search/label/Adventitious. (Accessed 12 July 2023).
[32] B.P. Payne, M.C. Biesinger, N.S. McIntyre, X-ray photoelectron spectroscopy studies of reactions on chromium metal and chromium oxide surfaces, J. Electron Spectrosc. Relat. Phenom. 184 (2011) 29–37, https://doi.org/10.1016/j.elspec.2010.12.001.
[33] G. Ning, R.L. Flemming, Rietveld refinement of $LaB_6$: data from μXRD, J. Appl. Crystallogr. 38 (2005) 757–759, https://doi.org/10.1107/S0021889805023344.
[34] H.M. Rietveld, A profile refinement method for nuclear and magnetic structures, J. Appl. Crystallogr. 2 (1969) 65–71, https://doi.org/10.1107/S0021889869006558.
[35] A.A. Coelho, TOPAS and TOPAS-Academic: an optimization program integrating computer algebra and crystallographic objects written in C++, J. Appl. Crystallogr. 51 (2018) 210–218, https://doi.org/10.1107/S1600576718000183.
[36] B. Hirschorn, M.E. Orazem, B. Tribollet, V. Vivier, I. Frateur, M. Musiani, Determination of effective capacitance and film thickness from constant-phase-element parameters, Electrochim. Acta 55 (2010) 6218–6227, https://doi.org/10.1016/j.electacta.2009.10.065.
[37] M. Bendova, Z. Pytlicek, J. Prasek, A. Mozalev, The growth and unique electronic properties of the porous-alumina-assisted hafnium-oxide nanostructured films, Electrochim. Acta 327 (2019) 135029, https://doi.org/10.1016/j.electacta.2019.135029.
[38] K. Kamnev, M. Sepúlveda, M. Bendova, Z. Pytlicek, J. Prasek, E. Kolibalova, J. Michalicka, A. Mozalev, The growth, composition, and functional properties of self-organized nanostructured $ZrO_2$-$Al_2O_3$ anodic films for advanced dielectric applications, Adv. Electron. Mater. 7 (2021) 2100505, https://doi.org/10.1002/aelm.202100505.
[39] S. Komiyama, E. Tsuji, Y. Aoki, H. Habazaki, M. Santamaria, F. Di Quarto, P. Skeldon, G.E. Thompson, Growth and field crystallization of anodic films on Ta–Nb alloys, J. Solid State Electrochem. 16 (2012) 1595–1604, https://doi.org/10.1007/s10008-011-1565-7.
[40] X-ray photoelectron spectroscopy (XPS) reference pages, Depth of analysis, inelastic mean free path. http://www.xpsfitting.com/search/label/Depth%20of%20Analysis. (Accessed 24 August 2023).
[41] G.E. Cavigliasso, M.J. Esplandiu, V.A. Macagno, Influence of the forming electrolyte on the electrical properties of tantalum and niobium oxide films: an EIS comparative study, J. Appl. Electrochem. 28 (1998) 1213–1219, https://doi.org/10.1023/A:1003449917148.
[42] H. Habazaki, T. Matsuo, H. Konno, K. Shimizu, K. Matsumoto, T. Takayama, Y. Oda, P. Skeldon, G.E. Thompson, Analysis of anodic films on Nb and $NbN_x$ by glow discharge optical emission spectroscopy, Surf. Interface Anal. 35 (2003) 618–622, https://doi.org/10.1002/sia.1583.
[43] H. Habazaki, T. Matsuo, H. Konno, K. Shimizu, S. Nagata, K. Matsumoto, K. Takayama, Y. Oda, P. Skeldon, G.E. Thompson, Influence of silicon species on the electric properties of anodic niobia, Electrochim. Acta 48 (2003) 3519–3526, https://doi.org/10.1016/S0013-4686(03)00473-0.
[44] H. Habazaki, M. Yamasaki, T. Ogasawara, K. Fushimi, H. Konno, K. Shimizu, T. Izumi, R. Matsuoka, P. Skeldon, G.E. Thompson, Thermal degradation of anodic niobia on niobium and oxygen-containing niobium, Thin Solid Films 516 (2008) 991–998, https://doi.org/10.1016/j.tsf. 2007.06.127.
[45] H. Störmer, A. Weber, V. Fischer, E. Ivers-Tiffée, D. Gerthsen, Anodically formed oxide films on niobium: microstructural and electrical properties, J. Eur. Ceram. Soc. 29 (2009) 1743–1753, https://doi.org/10.1016/j.jeurceramsoc.2008.10.019.
[46] A. Mozalev, M. Sakairi, H. Takahashi, H. Habazaki, J. Hubálek, Nanostructured anodic-alumina-based dielectrics for high-frequency integral capacitors, Thin Solid Films 550 (2014) 486–494, https://doi.org/10.1016/j.tsf.2012.02.077.
[47] N. Cabrera, N.F. Mott, Theory of the oxidation of metals, Rep. Prog. Phys. 12 (1949) 163–184, https://doi.org/10.1088/0034-4885/12/1/308.
[48] H. Masuda, M. Satoh, Fabrication of gold nanodot array using anodic porous alumina as an evaporation mask, Jpn. J. Appl. Phys. 35 (1996) L126–L129, https://doi.org/10.1143/JJAP.35.L126.
[49] K. Yasui, K. Nishio, H. Masuda, Fabrication of nanocomposites by filling nanoholes in highly ordered anodic porous alumina by vacuum deposition of metal, Jpn. J. Appl. Phys. 44 (2005) L1181–L1183, https://doi.org/10.1143/JJAP.44.L1181.
[50] Y. Park, Y. Saito, R. Pomprasertsuk, J. Cheng, S. Cha, F.B. Prinz, Electrical properties of YSZ thin films deposited on nanoporous substrates, ECS Proc. Vol. PV 2003-7 (2003) 169–180, https://doi.org/10.1149/200307.0169PV.
[51] J.P.S. Pringle, The anodic oxidation of superimposed metallic layers: theory, Electrochim. Acta 25 (1980) 1423–1437, https://doi.org/10.1016/0013-4686(80)87157-X.
[52] M.M. Lohrengel, Formation of ionic space charge layers in oxide films on valve metals, Electrochim. Acta 39 (1994) 1265–1271, https://doi.org/10.1016/0013-4686(94)E0046-3.
[53] V. Martinez, C. Besset, F. Monsieur, L. Montès, G. Ghibaudo, Modified space-charge limited conduction in tantalum pentoxide MIM capacitors, Microelectron. Eng. 84 (2007) 2310–2313, https://doi.org/10.1016/j.mee.2007.04.023.
[54] I. Vrublevsky, A. Jagminas, J. Schreckenbach, W.A. Goedel, Electronic properties of electrolyte/anodic alumina junction during porous anodizing, Appl. Surf. Sci. 253 (2007) 4680–4687, https://doi.org/10.1016/j.apsusc.2006.10.038.
[55] I. Vrublevsky, V. Parkoun, J. Schreckenbach, W.A. Goedel, Dissolution behaviour of the barrier layer of porous oxide films on aluminum formed in phosphoric acid studied by a re-anodizing technique, Appl. Surf. Sci. 252 (2006) 5100–5108, https://doi.org/10.1016/j.apsusc.2005.07.028.
[56] A. Mozalev, A.J. Smith, S. Borodin, A. Plihauka, A.W. Hassel, M. Sakairi, H. Takahashi, Growth of multioxide planar film with the nanoscale inner structure via anodizing Al/Ta layers on Si, Electrochim. Acta 54 (2009) 935–945, https://doi.org/10.1016/j.electacta.2008.08.030.
[57] A. Mozalev, H. Habazaki, J. Hubálek, The superhydrophobic properties of self-organized microstructured surfaces derived from anodically oxidized Al/Nb and Al/Ta metal layers, Electrochim. Acta 82 (2012) 90–97, https://doi.org/10.1016/j.electacta.2012.05.065.
[58] M. Sepúlveda, K. Kamnev, Z. Pytlicek, J. Prasek, A. Mozalev, Superhydrophobic-oleophobic visible-transparent antireflective nanostructured anodic $HfO_2$ multifunctional coatings for potential solar panel applications, ACS Appl. Nano Mater. 4 (2021) 1754–1765, https://doi.org/10.1021/acsanm.0c03202.
[59] Z. Fohlerova, A. Mozalev, Anodic formation and biomedical properties of hafnium-oxide nanofilms, J. Mater. Chem. B 7 (2019) 2300–2310, https://doi.org/10.1039/C8TB03180K.